



**HAL**  
open science

# Carboniferous-Permian tectono-metamorphic evolution of the Pelvoux Massif (External Crystalline Massif, Western Alps), with discussion on flow kinematics of the Eastern-Variscan Shear Zone

Kévin Fréville, Pierre Trap, Jonas Vanardois, Jérémie Melleton, Michel Faure, Olivier Bruguier, Marc Poujol, Philippe Lach

## ► To cite this version:

Kévin Fréville, Pierre Trap, Jonas Vanardois, Jérémie Melleton, Michel Faure, et al.. Carboniferous-Permian tectono-metamorphic evolution of the Pelvoux Massif (External Crystalline Massif, Western Alps), with discussion on flow kinematics of the Eastern-Variscan Shear Zone. *Bulletin de la Société Géologique de France*, 2022, 193, pp.13. 10.1051/bsgf/2022008 . insu-03678397v2

**HAL Id: insu-03678397**

**<https://insu.hal.science/insu-03678397v2>**

Submitted on 22 Aug 2022

**HAL** is a multi-disciplinary open access archive for the deposit and dissemination of scientific research documents, whether they are published or not. The documents may come from teaching and research institutions in France or abroad, or from public or private research centers.

L'archive ouverte pluridisciplinaire **HAL**, est destinée au dépôt et à la diffusion de documents scientifiques de niveau recherche, publiés ou non, émanant des établissements d'enseignement et de recherche français ou étrangers, des laboratoires publics ou privés.



Distributed under a Creative Commons Attribution 4.0 International License

# Carboniferous-Permian tectono-metamorphic evolution of the Pelvoux Massif (External Crystalline Massif, Western Alps), with discussion on flow kinematics of the Eastern-Variscan Shear Zone

Kévin Fréville<sup>1,2,3,\*</sup>, Pierre Trap<sup>2</sup>, Jonas Vanardois<sup>2</sup>, Jérémie Melleton<sup>3</sup>, Michel Faure<sup>1</sup>, Olivier Bruguier<sup>4</sup>, Marc Poujol<sup>5</sup> and Philippe Lach<sup>3</sup>

<sup>1</sup> UMR 7327, Institut des Sciences de la Terre d'Orléans, Université d'Orléans, CNRS, 45071 Orléans Cedex 2, France

<sup>2</sup> UMR 6249 Chrono-environnement, Université de Franche-Comté, 16 route de Gray, 25030 Besançon Cedex, France

<sup>3</sup> BRGM-French Geological Survey, 3 Avenue Claude Guillemin, 45100 Orléans, France

<sup>4</sup> Géosciences Montpellier, Université de Montpellier, CNRS, Place Eugène Bataillon, 34095 Montpellier Cedex 5, France

<sup>5</sup> Univ. Rennes, CNRS, Géosciences Rennes-UMRS 6118, 35000 Rennes, France

Received: 14 June 2021 / Accepted: 19 May 2022 / Publishing online: 22 August 2022

**Abstract** – Based on new structural, petrological and U-Th-Pb geochronological data, a reappraisal of the Variscan tectono-metamorphic history of the Pelvoux Massif (External Crystalline Massif, French Alps) is proposed with the aim to understand the flow pattern and kinematics of the Variscan partially molten crust and the Eastern Variscan Shear Zone. The Pelvoux Massif consists of high-grade metamorphic rocks of middle to lower crust, mostly migmatites, that record a prominent syn-metamorphic deformation event ( $D_2$ ) characterized by a pervasive NE-SW striking, steeply dipping,  $S_2$  foliation, and a network of anastomosed NS and NW-SE trending shear zones, the kinematics of which indicates a sinistral transpression. Relics of an early syn-metamorphic event ( $D_1/M_1$ ) related to crustal thickening and top-to-the-east nappe stacking are also reported. Both the  $D_1$  and  $D_2$  features are interpreted as reflecting a NW-SE shortening event, firstly marked by dominant nappe stacking, and secondly overprinted by a sinistral transpression that started at peak metamorphism with the onset of crustal partial melting at ca. 650 °C during the late Viséan (ca. 335–330 Ma). Ongoing sinistral  $D_2$  transpression in the partially molten middle-lower crust of the Pelvoux involved strain partitioning between C and C' shear zones and horizontal longitudinal flow in the range 330–300 Ma. Along the anatectic front, vertical shortening and top-to-the-NW shearing ( $D_3$ ) is coeval with  $D_2$  and argue for southeastward motion of the partially molten crust. The contemporaneity between NW-SE directed transpressional flow and vertical shortening is supported by our radiometric data of  $D_2$  and  $D_3$  and attests for strain partitioning between the suprastructure and infrastructure during horizontal crustal flow under transpressive regime. The exhumation of deep-seated rocks during sinistral transpression followed a near isothermal (ca. 700 °C) evolution down to pressure of ca. 0.5 GPa in the period 325–306 Ma. The sinistral transpression recorded in the Pelvoux Massif might corresponds to an antithetic shear zone coeval with the dextral East-Variscan Shear Zone, proposed for this part of the Variscan orogen.

**Keywords:** Variscan belt / Western Alps / Belledonne-Pelvoux / East-Variscan Shear Zone / migmatite / transpression

**Résumé** – **Évolution tectono-métamorphique Carbonifère-Permien du massif du Pelvoux (Massif cristallin externe, Alpes occidentales), avec discussion sur la cinématique de fluage de la zone de cisaillement Est Varisque.** Sur la base de nouvelles données structurales, pétrologiques et géochronologiques U-Th-Pb, une réévaluation de l'histoire tectono-métamorphique varisque du massif du Pelvoux (Massif cristallin externe, Alpes françaises) est proposée dans le but de comprendre le style et la cinématique du fluage de la croûte varisque partiellement fondue et de la Zone de Cisaillement Est Varisque. Le massif du Pelvoux est constitué de roches métamorphiques de haut grade, de la croûte moyenne à inférieure, principalement des migmatites, qui enregistrent un événement de déformation syn-métamorphique

\*Corresponding author: [kevin.freville@gmail.com](mailto:kevin.freville@gmail.com)

prédominant ( $D_2$ ) caractérisé par une orientation NE-SW, une foliation  $S_2$  à fort pendage et un réseau anastomosé de zones de cisaillement d'orientation NS et NW-SE dont la cinématique indique une transpression senestre. Des reliques d'un événement syn-métamorphique précoce ( $D_1/M_1$ ) lié à l'épaississement de la croûte et à l'empilement des nappes à vergence Est sont retrouvées. Les caractéristiques de  $D_1$  et  $D_2$  sont interprétées comme reflétant un événement de raccourcissement NW-SE, d'abord marqué par l'empilement dominant des nappes, qui évolue ensuite en une transpression senestre, initiée au pic du métamorphisme avec le début de l'anatexie crustale dès 650 °C, à la fin du Viséen (335–330 Ma). Dans la croûte partiellement fondue, la déformation transpressive senestre  $D_2$  se partitionne avec la formation de zones de cisaillement C et C' qui accommodent le fluage longitudinal entre 330 et 300 Ma. Le long du front anatectique, un raccourcissement vertical accompagné d'un cisaillement vers le NW (déformation  $D_3$ ) sont contemporains de  $D_2$  et participent aussi à l'échappement vers le sud-est de la croûte partiellement fondue. La contemporanéité entre le fluage transpressif dirigé NW-SE ( $D_2$ ) et le raccourcissement vertical à cinématique NW ( $D_3$ ) est étayée par nos données radiométriques. L'exhumation des roches profondes lors de la transpression senestre a suivi une évolution quasi isotherme (~ 700 °C) jusqu'à une pression d'environ 0,5 GPa dans la période 325–306 Ma. La transpression senestre enregistrée dans le massif du Pelvoux pourrait correspondre à une zone de cisaillement antithétique contemporaine de la zone de cisaillement dextre Est-Varisque.

**Mots clés :** chaîne Varisque / Alpes occidentales / Belledonne-Pelvoux / zone de cisaillement Est varisque / migmatite / transpression

## 1 Introduction

Together with the Maures-Corsica-Sardinia Massifs, the External Crystalline Massifs (ECMs), exposed in the Helvetic Zone of the Western Alpine belt represent the Eastern Branch of the Variscan orogen (Fig. 1). In spite of several geodynamic interpretations (Fernandez *et al.*, 2002; Corsini and Rolland, 2009; Guillot and Ménot, 2009; Rossi *et al.*, 2009; Von Raumer *et al.*, 2013; Faure *et al.*, 2014; Oliot *et al.*, 2015; Faure and Ferrière, 2022), the timing of the main tectono-metamorphic events in the ECMs, and the correlations between these massifs remain poorly constrained mainly because of a strong imprint by late-orogenic transpressional tectonics during Carboniferous time and intense partial melting and plutonism in the mid-lower crust at that time. Widespread Carboniferous crustal partial melting in response to thermal relaxation (*i.e.*, Alcock *et al.*, 2015; Barbey *et al.*, 2015; Villaros *et al.*, 2018) triggered horizontal flow of the lower and middle crust (Cochelin *et al.*, 2017; Vanderhaeghe *et al.*, 2020) and strain partitioning along strike-slip shear zone and exhumation of migmatitic domes (Vanderhaeghe *et al.*, 1999; Ledru *et al.*, 2001). In the ECMs, the structural and kinematic feature associated with partial melting and magmatism are still elusive.

The Eastern Crystalline Massifs (ECMs) stand out as a complex portion of the European Variscan Belt that was built along a major crustal-scale wrenching corridor, named the East Variscan Shear Zone EVSZ (Fig. 1A; EVSZ; Corsini and Rolland, 2009; Guillot and Ménot, 2009; Rolland *et al.*, 2009; Carosi *et al.*, 2012; Padovano *et al.*, 2012, 2014; Simonetti *et al.*, 2018). The EVSZ is considered as the main structure that accommodated the shaping of the variscan eastern orocline (Fig. 1A; Matte, 2001; Bellot, 2005; Ballèvre *et al.*, 2018). A series of multidisciplinary studies have provided many structural, petrological, and radiometrical data in that part of the East Variscan branch that was affected by the EVSZ (Guillot and Menot, 2009), *i.e.*, the Aiguilles-Rouges and Mont-Blanc Massif (Von Raumer and Bussy, 2004; Von Raumer *et al.*, 2013; Simonetti *et al.*, 2020a), the Belledonne-Pelvoux Massifs (Guillot and Menot, 2009), the

Argentera Massif (Simonetti *et al.*, 2018, 2021), the Maures-Tanneron Massif (Rolland *et al.*, 2009; Schneider *et al.*, 2014; Gerbault *et al.*, 2018; Simonetti *et al.*, 2020b), and Sardinia (Carosi *et al.*, 2012) showing that the EVSZ was responsible for complex strain partitioning in time and space during Carboniferous. Simonetti *et al.* (2020a) proposed the first detailed picture of the EVSZ with the position, orientation and kinematics of the major branches constituting the regional-scale anastomosed system (Fig. 1B). Because not all ECMs are considered in the EVSZ system, the location, thickness and internal strain pattern of the EVSZ remains elusive as well as the variations of strain regimes and kinematics that are expected to exist at lithospheric scale.

In this contribution we focus on the Belledonne-Pelvoux area that is a large but still poorly understood portion of the ECMs, and absent from the reconstruction of the EVSZ anastomosed system (Fig. 1B). The Pelvoux Massif displays a well exposed section of the late-Variscan low and middle crust mainly composed of migmatites and granites formed in response to a crustal melting event developed at the end of a HT low-to-medium pressure Carboniferous metamorphism (Pecher, 1970; Le Fort, 1973). There, a sinistral kinematics was documented (Strzeczynski *et al.*, 2005) making it unique in the transpressive framework of the ECMs where dextral shearing dominates (Corsini and Rolland, 2009; Guillot and Ménot, 2009; Rolland *et al.*, 2009; Carosi *et al.*, 2012; Padovano *et al.*, 2012, 2014; Simonetti *et al.*, 2018, 2020a).

Presently, the Pelvoux Massif lacks large-scale structural analysis combined with quantified tectono-metamorphic evolution using modern petrological methods. Simonetti *et al.* (2018, 2020a, 2020b) suggested that dextral transpression in the ECMs was initiated at ca. 320 Ma with the exception of the Argentera Massif where it could have started at ca. 330–340 Ma. In the Pelvoux Massif, rare geochronological data document the protolith age of some orthogneiss, but the syn-metamorphic deformation is still undated. A study of the Pelvoux Massif will help integrating the sinistral kinematics in the general framework of the dextral

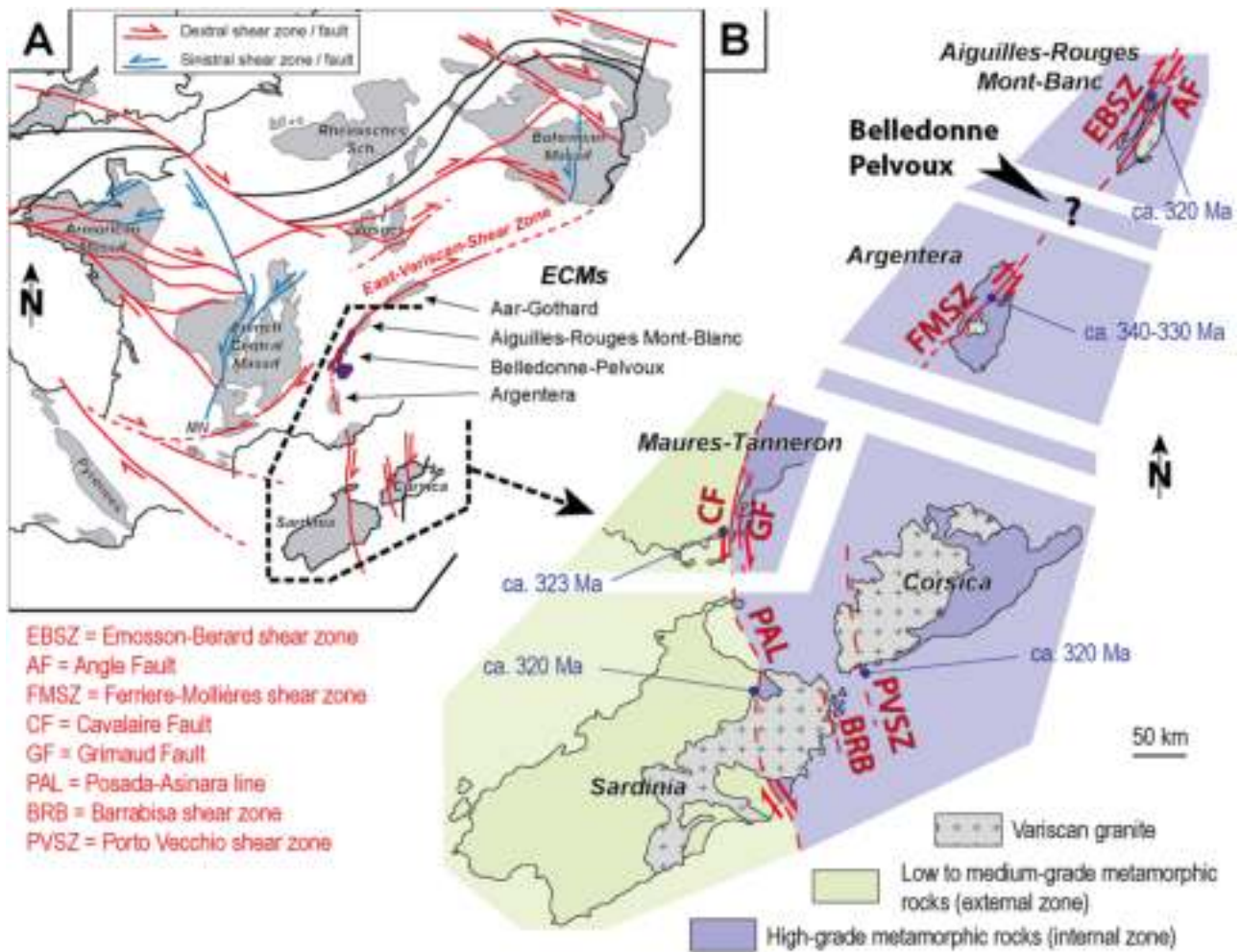


**Fig. 1.** (A) Location of the External Crystalline Massif (ECMs) within the Variscan framework, modified after Franke *et al.* (2017). (B) State-of-the-art concept showing the possible shear zone pattern along the ECMs and Corsica-Sardinia, in relation with the dextral EVSZ (modified from Simonetti *et al.*, 2020). The studied area, *i.e.*, the Belledonne-Pelvoux Massif, is not yet considered in this scheme.

transpression model of the EVSZ (*e.g.*, Simonetti *et al.*, 2020a) and of the whole Variscan belt (*e.g.*, Ballèvre *et al.*, 2018; Edel *et al.*, 2018).

In this article, we present (i) the detailed finite strain pattern at the transition from the upper crust and the former partially molten crust that crops out in the Pelvoux Massif and (ii) microstructural, petrological and geochronological analyses on samples from the unmolten and molten crust. These results allow us to discuss (i) the P-T-D-t evolution recorded in some high-grade metamorphic rocks; (ii) the geometrical and temporal relationships between deformation, metamorphism, partial melting, and magma emplacement; (iii) the kinematics of ductile flow in the mid-crust. Our findings are compared to those recently obtained on the adjacent Belledonne Massif by Fréville *et al.* (2018) and Jacob *et al.* (2021) and enable us to propose a tectono-metamorphic evolution model of the Pelvoux that may represent an antithetic branch of the EVSZ.

## 2 Geological setting

### 2.1 Overview of the Variscan Belt in the Alpine Crystalline Massifs

The Variscan belt formed in response to collision between Gondwana and Laurussia continents, and several Gondwana-derived microcontinents during the Late Devonian to Early Carboniferous (Fig. 1A), (Autran and Cogné, 1980; Paris and Robardet, 1990; Matte, 1991, 2001, 2007; Tait *et al.*, 1997, 2000; Franke, 2000; Von Raumer *et al.*, 2003; Faure *et al.*, 2005; Stampfli *et al.*, 2013). From Late Visean to Early Permian, thermal relaxation and mafic to felsic plutonism enhanced a widespread partial melting of the thickened low-middle crust, that modified gravity vs. boundary stress balance and enhanced a complex intracontinental strain partitioning in a global transpressive regime (*e.g.*, Henk *et al.*, 2000; Rabin *et al.*, 2015; Cochelin *et al.*, 2017).

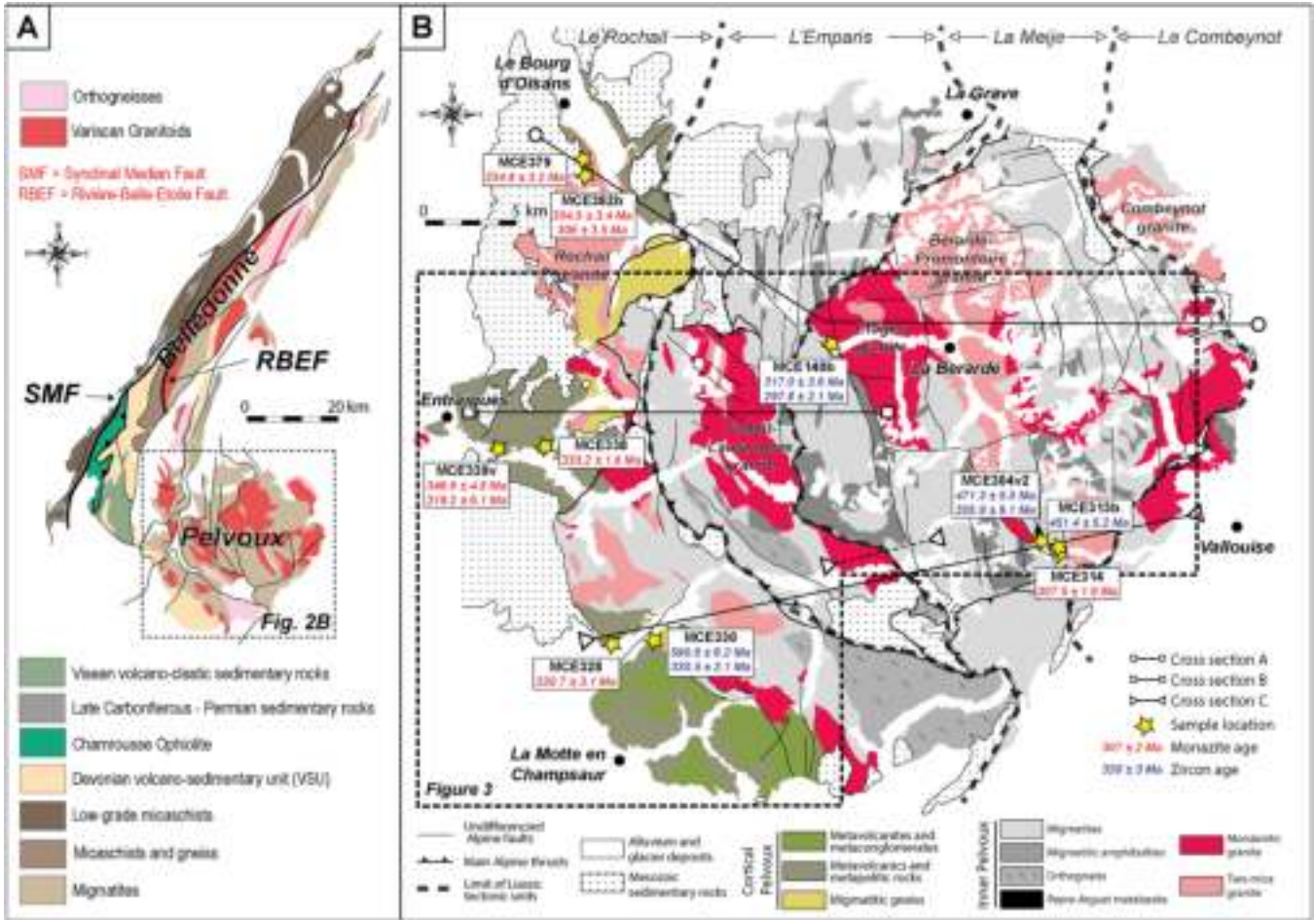


**Fig. 2.** (A) Simplified Geological map of the ECMs. Dashed square shows the extent of Figure 2B. (B) Geological map of the Pelvoux Massif with sample location. Dashed area shows the location of Figure 3.

In its present geometry, the External Crystalline Massifs (ECMs) of the Alps form an arcuate, concave to the East, branch of the Variscan belt that includes, from North to South, the Aar-Gothard, Aiguilles-Rouges-Mont Blanc, Belledonne, Grandes Rousses, Pelvoux, and Argentera Massifs (Fig. 1B) (e.g., Barfety *et al.*, 2000; Guillot and Ménot, 2009). A first-order three-fold subdivision, previously proposed by Bordet and Bordet (1963), and Guillot and Ménot (2009; Fig. 1B), defines the Western, Central and Eastern domains.

The Western domain consists of slightly metamorphosed micaschists and metagreywackes considered as a turbiditic series of Ordovician age (Bordet and Bordet, 1963; Fréville *et al.*, 2018). The central domain, including the SW part of the Aiguilles-Rouges, the SW part of Belledonne Massifs, and the western part of the Pelvoux Massif or Cortical Pelvoux area (Le Fort, 1973; Fig. 2) is made of a stack of several lithotectonic units, namely from top to bottom: (i) the Cambro-Ordovician Chamrousse ophiolite (Carne, 1965a, 1965b, 1970; Bodinier *et al.*, 1981; Ménot, 1987, 1988a, 1988b; Pin and Carne, 1987); (ii) an amphibolitic facies gneiss, micaschists and volcano-sedimentary rocks (VSU, Riouperoux-Livet and Allemont units) overlain by (iii) a weakly

metamorphosed and deformed conglomerate, black schist, and acidic volcanic rocks, named the Taillefer unit (Gibery, 1968; Ménot, 1988; Fréville *et al.*, 2018).

The Eastern part of the ECMs consists of high-grade rocks of the mid-lower crust with migmatites enclosing several lenses of HP granulites and retrogressed eclogites that crop out in the Argentera Massif, the Inner Pelvoux area, the NE Belledonne area, the major part of the Aiguilles-Rouges-Mont Blanc Massif, and the Aar-Gothard Massif (Fig. 1B, Paquette *et al.*, 1989; Abrecht and Biino, 1991; Lombardo *et al.*, 1997; Von Raumer and Bussy, 2004; Ferrando *et al.*, 2008; Compagnoni *et al.*, 2010; Rubatto *et al.*, 2010; Jacob *et al.*, 2021). These three crustal domains are juxtaposed along the Synclinal-Median Fault (SMF) and the Rivier-Belle Etoile Fault (RBEF, Fig. 1B).

## 2.2 Impact of the post-variscan reworking in the Belledonne-Pelvoux area

The Jurassic rifting, coeval with the opening of the Liguro-Piemonte ocean, was responsible for the development of brittle normal faults associated with the local tilting of the Palaeozoic

basement. It was responsible for the individualization of several Liassic blocks. These are the La Mure and Le Taillefer blocks within the Belledonne Massif, and Le Rochail, L'Emparis, La Meije, and Le Combeynot blocks in the Pelvoux Massif (Fig. 2) (Lemoine *et al.*, 1986; Barfety *et al.*, 1988; Lemoine, 1988). The Miocene Alpine deformation inverted the Jurassic normal faults and was responsible for the development of localized NW-SE trending shear zones with a top-to-the-NW ductile shearing (Bellahsen *et al.*, 2014; Bellanger *et al.*, 2014, 2015; Boutoux *et al.*, 2014). The Alpine shortening in the Palaeozoic basement was coeval with a weak metamorphic overprint in the prehnite-pumpellyite to greenschist facies. Outside these localized Alpine shear zones, the markers of the Pre-Alpine tectono-metamorphic events are particularly well-preserved in the Belledonne-Pelvoux area.

### 2.3 Summary of previous P-T-t data on the Pelvoux Massif

In the literature, the Pelvoux Massif is described as two-fold, with the Cortical and the Inner Pelvoux domains, the boundary of which is mainly reworked by alpine faulting (Le Fort, 1973). The Cortical Pelvoux, located in the western part, consists of an alternation of volcanoclastic rocks and micaschists with migmatitic gneisses at the base of these series (Fig. 2). Barrovian metamorphism is attested by kyanite-staurolite bearing micaschists documented in the Cortical Pelvoux (Le Fort, 1973) but quantitative thermobarometric estimates are not available. In the adjacent SW Belledonne, a MP-HT barrovian metamorphism ( $M_1$ ) is documented with P-T conditions at ca. 0.5–0.6 GPa, 600 °C, recorded in staurolite-bearing micaschists and up to ca. 0.8 GPa, 680 °C for the migmatitic gneiss in lowest unit (Guillot and Ménot, 1999; Fernandez *et al.*, 2002; Fréville *et al.*, 2018). The  $M_1$  metamorphism is coeval with a  $D_1$  deformation characterized by the development of a westward dipping foliation  $S_1$  and E-W stretching  $L_1$  lineation interpreted as an eastward nappe stacking event (Fréville *et al.*, 2018). At upper structural level in the Cortical Pelvoux, a series of micaschists and volcanoclastic rocks is overlain by black schists and conglomerates, similar to the Taillefer unit observed in SW Belledonne (Barfety *et al.*, 2000; Guillot and Ménot, 2009) (Fig. 2).

The Inner Pelvoux is composed of i) migmatites that developed through partial melting of paragneiss, orthogneiss and amphibolites, and ii) several generations of granitoids (Pecher, 1970; Le Fort, 1973). Some mafic lenses (*e.g.*, Peyre-Arguet, Fig. 2) within migmatitic paragneiss record amphibolite facies P-T conditions of  $0.7 \pm 0.1$  GPa,  $650 \pm 50$  °C, and a low-pressure granulite facies of  $0.5 \pm 0.1$  GPa,  $800 \pm 50$  °C, followed by a retrogressive evolution in the greenschist facies conditions (Grandjean *et al.*, 1996). Granulitic conditions have also been inferred from the migmatitic gneiss (Pecher, 1970; Pecher and Vialon, 1970) but without any phase diagram quantification. Two episodes of partial melting are recognized with a first low-temperature, cordierite-free migmatite, and a high-temperature–low-pressure, cordierite-bearing migmatite (Bogdanoff *et al.*, 1991). In the Inner Pelvoux, the foliation is mostly steeply dipping to vertical, but superimposed deformation has been invoked (Pecher, 1970; Le Fort, 1973) and the

relationships between partial melting and deformation are still unclear.

Two groups of granitoids are distinguished, namely two-mica granites and monzonitic granites (Barfety *et al.*, 1982; Debon and Lemmet, 1999). Presently, only the two-mica Rochail and Combeynot granites, and the Turbat-Lauranoure monzonite have been dated with proposed emplacement age at  $343 \pm 11$  Ma,  $312 \pm 7$  Ma and  $302 \pm 2$  Ma, respectively (U-Pb on zircon; Canic, 1998; Guerrot and Debon, 2000). N-S to NW-SE striking, syn-magmatic sinistral C-S fabrics are described in granitic plutons (Strzeczynski *et al.*, 2005) but the geometrical and kinematic relationships with their migmatitic host rocks are poorly understood.

## 3 Structural analysis

### 3.1 Strain patterns in the metamorphic and migmatitic pile

At the scale of the entire Pelvoux Massif, field observations show that the dominant macroscopic ductile structure is a steeply dipping foliation, ascribed here to the  $D_2$  event (Figs. 3 and 4). Due to its pervasive character, the  $D_2$  event will be presented first.

#### 3.1.1 The $D_2$ submeridian sinistral shearing

The majority of this  $D_2$  planar structure is represented by a gneissic (*i.e.*, solid-state deformation), and a migmatitic foliation (*i.e.*, suprasolidus deformation). It ranges from NW-SE to NE-SW with the occurrence of three main directional populations:  $\sim N30^\circ E$ ,  $\sim N140^\circ E$  and  $\sim N170^\circ E$  (Figs. 3 and 4). The  $\sim N30^\circ E$  foliation is less represented than the two other directions and is referred to as  $S_2$  in the following.  $S_2$  is axial planar to upright folds  $F_2$  that deform an earlier weakly dipping  $S_1$  foliation (see below).  $S_2$  developed in response to an E-W to NW-SE bulk shortening (Figs. 5A and 5B). In the Inner Pelvoux,  $S_2$  consists of a migmatitic layering that almost totally transposes  $S_1$  that is only preserved within  $F_2$  folds hinges (see next paragraph and Fig. 5C).

The two most developed  $D_2$  planar fabrics are striking  $N170^\circ E$  and  $N140^\circ E$  with a high ( $> 70^\circ$ ) dip angle (Fig. 3). Both sets show melt-present and solid-state deformation features (Fig. 5D). When the three directional populations of planar fabrics, *i.e.*,  $\sim N30^\circ E$ ,  $\sim N140^\circ E$  and  $\sim N170^\circ E$  are observed on the same outcrops, the cross-cutting relationships clearly indicate that the  $\sim N170^\circ E$  planar surface is a shear plane that reworks the  $\sim N30^\circ E$  directed foliation, and that both  $\sim N30^\circ E$  and  $\sim N170^\circ E$  trending planar surfaces are reworked by the  $\sim N140^\circ E$  shear zone, as portrayed in Figure 7.

In the northern and eastern portions of the Emparis and La Meije Blocks, the  $N170^\circ E$  trending and highly penetrative planar surface forms 100 meters to several kilometers wide shear zones (Figs. 3 and 4) along which a southward low-angle plunging  $L_2$  stretching lineation is observed (Fig. 3B). A sinistral kinematics is deduced from the observation of sigmoidal minerals or aggregates and the deflection of  $S_2$  (Figs. 3, 5E, 5F and 6A). In the southern part of the Pelvoux Massif, similar meter to kilometers sized sinistral high-strain corridors strike mostly  $\sim N140^\circ E$  (Fig. 3). Where the NW-SE planar fabric becomes preponderant, the N-S surface is only

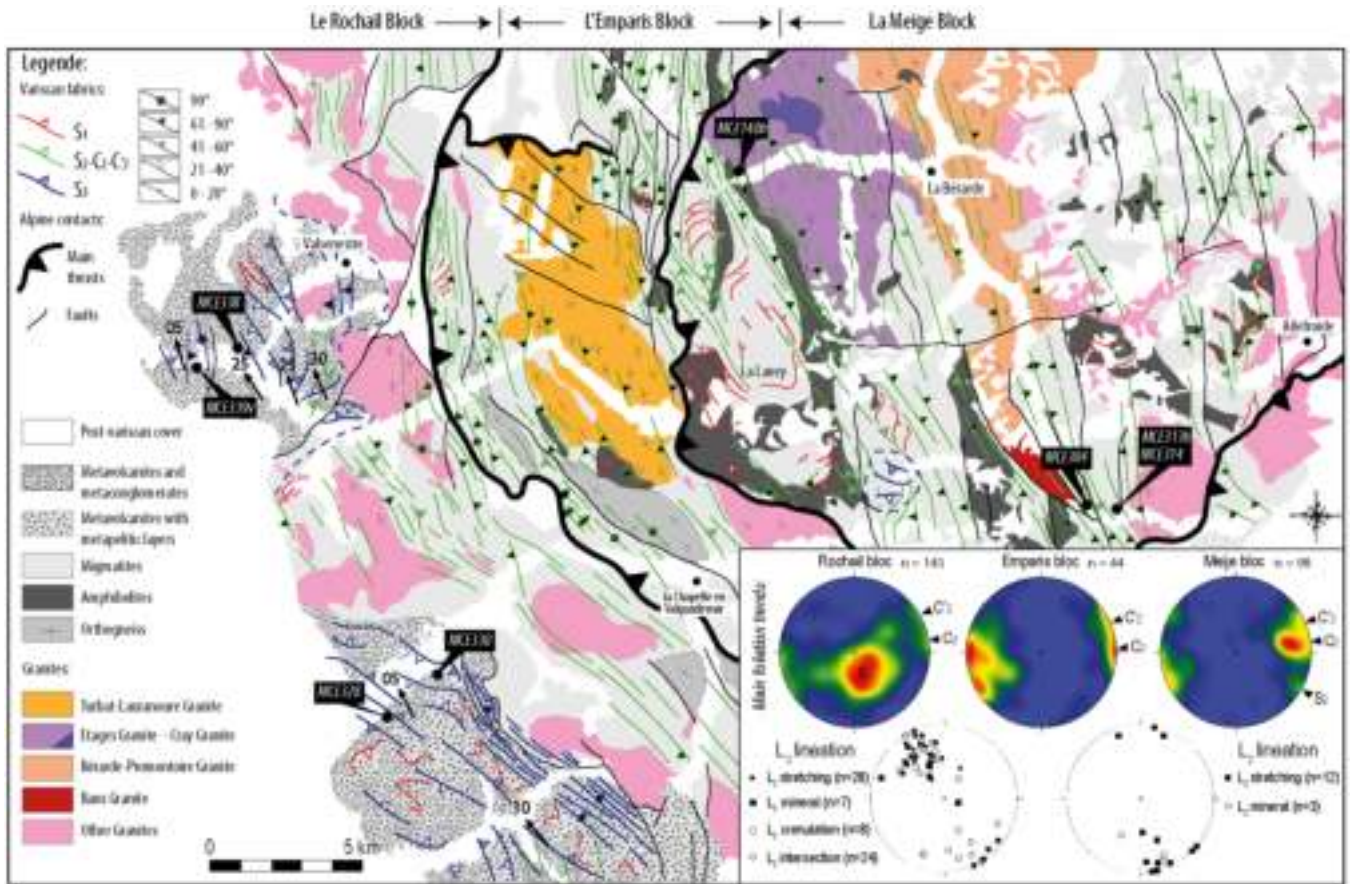


**Fig. 3.** Structural map of the Pelvoux Massif showing the heterogeneous Variscan strain pattern. Lower-hemisphere Wulff stereographic plots of poles of foliations and strikes of lineation.

preserved within centimeter to meter scale lenticular bodies (Fig. 7A). The mineral and/or stretching lineations are rarely observed; but when it is the case, they are sub-horizontal or moderately plunging (Fig. 3). In some places, within stromatic migmatite, the oblate shape of mafic restites suggests that flattening strain without the development of a preferred stretching direction was dominant (Fig. 6B). At the outcrop scale, some conjugate dextral and sinistral shear bands are also observed (Fig. 6C). Considering the geometric and kinematic features of the  $D_2$  structures, it appears that the  $N170^\circ E$  and  $N140^\circ E$  planar surfaces might be considered as  $C_2$  and  $C'_2$  shear planes that developed synchronously with  $S_2$  in a bulk sinistral strike-slip regime. This  $S_2$ ,  $C_2$ ,  $C'_2$  anastomosing system is observed from kilometer to meter scale (Fig. 3). The presence of leucosome within the  $S_2$ ,  $C_2$  and  $C'_2$  shear bands attests for the onset of  $D_2$  in a partially molten rock, under supra-solidus conditions (Fig. 5). Diatexite commonly shows rafts and schollens with a high aspect-ratio parallel to the migmatitic foliation arranged either on the  $C_2$  or  $C'_2$  trends (Figs. 6D–6F). In some places, cm-scale elongated cordierite aggregates are preferentially aligned along  $C_2$  and  $C'_2$  planes (Fig. 6F) indicating that low-pressure/high-temperature partial melting was coeval with the  $D_2$  sinistral strike-slip. The  $D_2$  planar surface is also reported within garnet-bearing amphibolites (Fig. 7B) that are interpreted as retrogressed HP granulites (Grandjean *et al.*, 1996).

### 3.1.2 The relictual $D_1$ structure

The  $D_2$  anastomosed system reworks a nearly horizontal or westward shallowly dipping early foliation, named  $S_1$  (Figs. 3 and 4). Within the Inner Pelvoux, the relictual  $S_1$  foliation corresponds to a gneissic layering and lithological alternations, the attitude of which marks large scale  $F_2$  folds. This is exemplified by the attitude of the La Lavey amphibolite formation in the La Meije block where a low angle ( $20^\circ$ – $40^\circ$ )  $S_1$  foliation is observed (Fig. 3). In the Inner Pelvoux, the  $S_1$  foliation only remains as isolated  $F_2$  fold hinges (Figs. 5A and 5B). In the Cortical Pelvoux, a  $S_1$  gneissic layering with a low-angle dip is also recognized. It is worth noting that  $L_1$  lineation is very rare with no clear preferred direction. Generally, the superimposition of  $S_2$  and  $S_3$  over  $S_1$  makes the latter difficult to depict in the outcrop. Relics of  $S_1$  are best recognized at the cm-scale (thin section; Fig. 8B).

### 3.1.3 Late horizontal shearing: $D_3$ structure

A flat-lying foliation ( $S_3$ ) superimposed on both the  $D_1$  and  $D_2$  fabrics is observed in the Inner Pelvoux, at m-cm scale, and attributed here to a  $D_3$  deformation (Figs. 3, 4 and 8). The  $D_2$  planar fabric elements ( $S_2$ - $C_2$ - $C'_2$ ) are involved in the formation of  $S_3$  axial planar  $F_3$  folds, and  $C_3$  shear bands with top-to-the-NW kinematics (Figs. 8 and 9). The attitude of

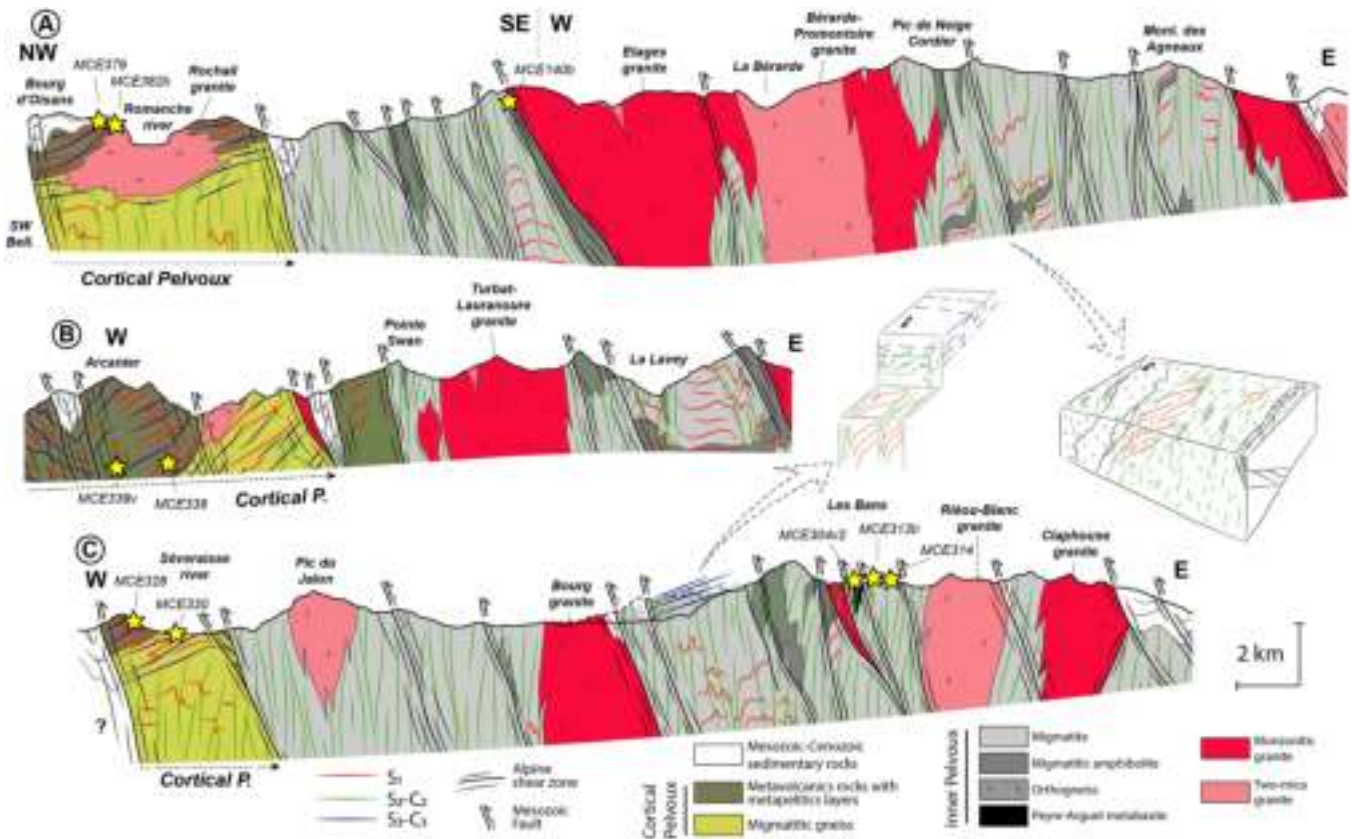


**Fig. 4.** (A) NW-SE cross-section through the northern part of the Pelvoux Massif. (B) E-W cross-section through the western part of the Pelvoux Massif. (C) W-E cross-section through the central part of the Pelvoux Massif.

leucosome that parallels  $S_3$  and the horizontal axial plane of  $F_3$  folds argue for melt migration during  $D_3$  (Figs. 9A and B). The melt-bearing  $S_3$  foliation cuts across  $S_2$  the upper structural level of the *La Meije* block.

In the *Le Rochail* block, a similar  $D_3$  strain pattern is observed with centimeter-scale  $F_3$  folds, with sub-horizontal axial planes that rework the subvertical  $S_2$  foliation.  $F_3$  fold axes are weakly plunging toward the NW. In the Cortical Pelvoux, a kilometer-scale  $D_3$  decreasing strain gradient can be observed from west to east. The  $S_3$  becomes more penetrative and presents a mylonitic fabric in which a  $N150-160^\circ E$  stretching lineation  $L_3$  is observed (Figs. 3 and 8D). Along the  $L_3$  stretching lineation, kinematic criteria (sigmoidal structures, pressure shadow, and shear bands) indicate a top-to-the-northwest sense of shear whatever the observation scale (Figs. 8 and 9). A-type folds with axes parallels to  $L_3$  lineation can be also observed. Accordingly, a similar stretching direction is documented by Jacob (2022) and Jacob *et al.* (2022) in the *La Meije* Block with the observations of a syn-migmatitic flat-lying foliation documenting a  $N150-N180$  directed horizontal flow that reworks early  $D_1$  and  $D_2$  fabrics.

### 3.2 Strain patterns in the felsic plutons

Within the granitic bodies of the Inner Pelvoux area (e.g., Turbat-Lauranoure, Etages, La Béarde-Promontoire

plutons), the  $S_1$ ,  $S_2$  and  $S_3$  were not identified but the two  $C_2$  ( $\sim N170^\circ E$ ) and  $C'_2$  ( $N140^\circ E$ ) structures are recognized. The preferred orientation of feldspar, biotite and shape ratio of mafic enclaves define a  $\sim N160-170^\circ E$  striking subvertical magmatic foliation. When observed, the stretching lineation is sub-horizontal and trends NNW-SSE as previously described by Strzeczynski *et al.* (2005). In agreement with these authors, we also document the presence of  $N135-140^\circ E$  striking and vertical ductile shear bands. These shear-bands rise to C-S-like structures, which reflect a sinistral strike-slip shearing, as best exemplified in the Bérarde-Promontoire and Etages granites (Fig. 3). In agreement with Strzeczynski *et al.* (2005), we consider that the sinistral kinematics was coeval with pluton emplacement. These  $C_2$  and  $C'_2$  planar surfaces that developed under supra-solidus magmatic conditions, appear in continuity with the  $D_2$  structures observed in the country rocks, indicating a syn- $D_2$  emplacement of those plutons.

In the northern part of the Cortical Pelvoux, the Rochail granite shows a sub-horizontal magmatic foliation inferred from biotite arrangement (Barfety *et al.*, 1988) and does not show subsolidus deformation. The  $D_2$  deformation was not observed in the pluton, and the  $S_3$  foliation wraps around the granite (Fig. 4A). This may indicate that the flat-lying magmatic foliation could be ascribed to  $S_1$  (see discussion below in Sect. 5).





**Fig. 5.** Field pictures of  $D_2$  folding and shearing. (A and B)  $F_2$  folding of migmatitic  $S_1$  and development of  $N30^\circ E$  trending  $S_2$  foliation as axial surface or transposition layering. (C and D) Folding and shearing along the  $C_2$  and  $C'_2$  trend (NS and NW-SE). The folded and sheared foliation is a  $S_1$ ,  $S_2$  or  $C_2$  planar surface. In photograph 5C, the gneissic protolith was folded when the anatectic melt was present, and the melt also migrated along  $D_2$  shear zone that parallels the axial plane. In 5D, shearing parallel to the axial plane resulted in solid-state recrystallization. (E) Diatexite with a high proportion of leucocratic neosome with metamafic layers showing  $D_2$  folding and sinistral shearing along a  $N120^\circ E$  trending  $C'_2$  syn-melt shear zone. (F) Schollen diatexite with meter scale metamafic enclaves stretched along N-S direction ( $C_2$ ) and shearing by a NW-SE trending  $C'_2$  infilled by melt. Location of outcrop photographs is given in Figure 2.

#### 4 Petro-chronological results

This section presents U-Th-Pb radiometric analyses of monazite and zircon grains from (1) mylonitic gneiss (samples *MCE379* and *MCE382b*), (2) Al-rich metapelites (samples *MCE339v*, *MCE338* and *MCE328*), (3) migmatites (samples *MCE314*, *MCE330*, *MCE140b* and *MCE313b*) and (4) metamafics (sample *MCE304v2*) sampled in the Cortical and Inner Pelvoux (Fig. 2; Tab. 1). A petrological description is given for each sample (Fig. 10). Before isotopic analyses, cathodoluminescence (CL) and back-scattered electron (BSE) images were acquired for all zircon and monazite grains, respectively, using a scanning electron microscope (SEM) in order to check spot locations with respect to the internal microstructures, inclusions, fractures and physical defects. For monazite, U-Th-Pb analyses were performed by LA-ICP-MS directly in thin section at the University of Montpellier (samples *MCE338*, *MCE314* and *MCE382b*) and at BRGM

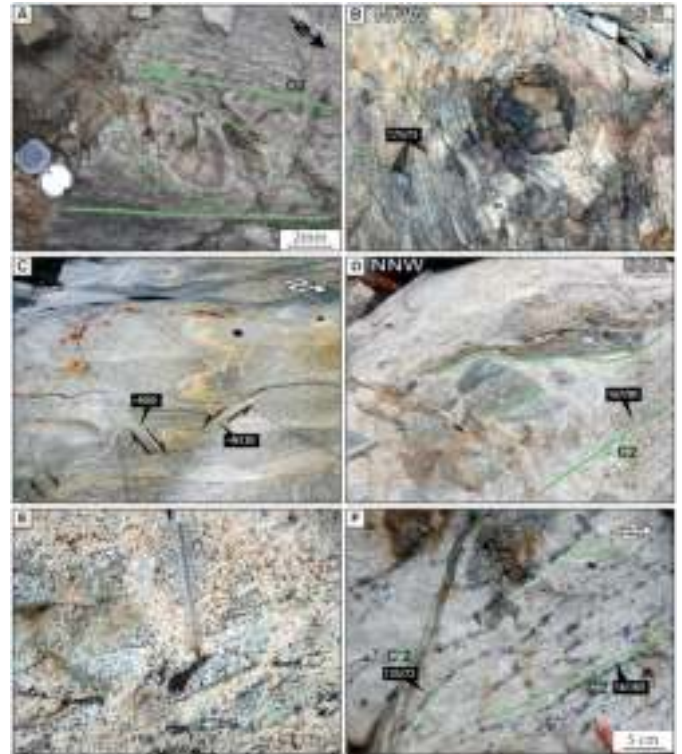


**Fig. 6.** Field pictures of  $D_2$  deformation synchronous with partial melting. (A) Sigmoidal quartz-rich resistor within  $D_2$  metatexite indicating sinistral shearing along  $C_2$  directed migmatitic foliation. (B) Oblate metamafic enclave observed in the XY-section within a stromatic diatexite. (C) Conjugate melt-bearing dextral and sinistral shear bands within heterogeneous diatexite. Main foliation is subvertical and trends ca.  $N170^\circ E$ . (D) Schollen diatexite migmatite developed from a hornblende-bearing volcano-sedimentary protolith. (E) Close-up on Figure 6D showing the dioritic to tonalitic composition of the leucocratic material containing various proportions of hornblende, some pyroxenes are also observed. The pen points to a garnet + hornblende rich schlieren. (F) Metatexite migmatite showing two sets of late cordierite-bearing leucosome, one set parallels the main foliation trends ( $\sim N15^\circ E$ , *i.e.*,  $C_2$ ) and the other one is oblique to the foliation, and oriented  $\sim N135^\circ E$  ( $C'_2$ ).

(Bureau de Recherche Géologique et Minière) (*MCE328*, *MCE339v* and *MCE379*) (Tab. S1). The analytical protocol for the University of Montpellier followed the procedure described in Bruguier *et al.* (2017) and is presented in Table S2. Manangotry (Poitrasson *et al.*, 2000) and Moacyr (Goncalves *et al.*, 2016) monazites used as calibration and quality control reference materials yielded concordia ages of  $552 \pm 2$  Ma (MSWD = 2.2,  $n = 38$ ) and  $507 \pm 2.5$  Ma (MSWD = 0.02,  $n = 14$ ), respectively. The analytical protocol for the BRGM is presented in Table S3 and the Madmon and Namaqualand monazites used as quality control reference materials yielded concordia ages of  $514 \pm 7$  Ma (MSWD = 1.4,  $n = 10$ ) and  $994 \pm 17$  Ma (MSWD = 1.3,  $n = 10$ ), respectively.

The zircon U-Pb analyses were performed at BRGM (samples *MCE330*, *MCE304v2* and *MCE313b*) and at GeO-HeLiS analytical platform (University Rennes 1) (sample

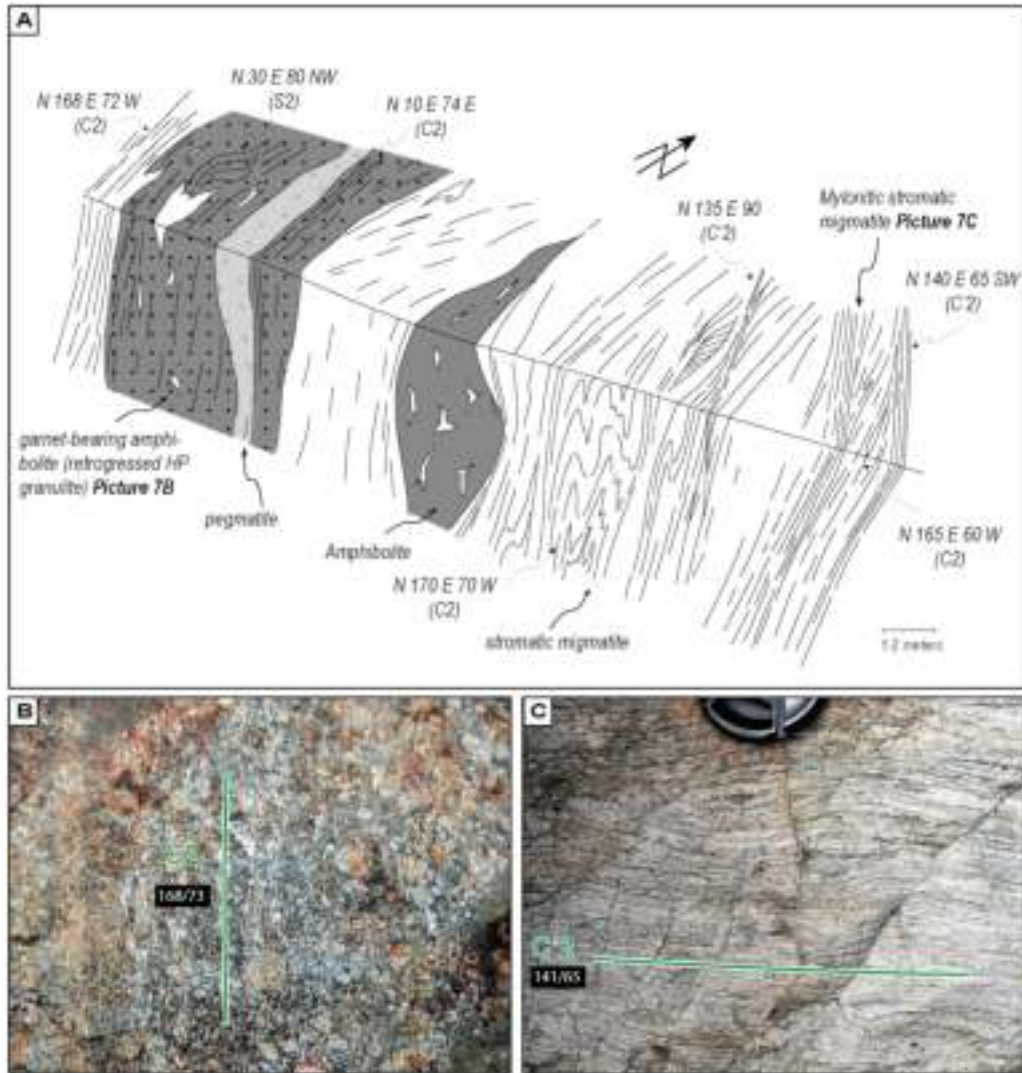


**Fig. 7.** (A) Schematic drawing showing the three main trends of the  $D_2$  planar surface arranged in a sinistral  $S_2$ - $C_2$ - $C'_2$  like anastomosed transpressional system. This representative outcrop comes from the Bans valley, southeastern Inner Pelvoux. (B) Picture 7B shows the steeply dipping  $S_2$  cleavage observed within the Peyre-Arguet mafic granulite, retrogressed into amphibolite. Very thin seams of leucosome are located parallel to the compositional layering, and  $S_2$  or  $C_2$  foliation. (C) Picture 7C shows a strongly layered stromatic migmatite that has been reworked by solid-state deformation during sinistral shearing along a  $C'_2$  plane.

*MCE140b*, Tabs. S1 and S4). Zircon grains were obtained by a conventional mineral separation. The selected grains (~100–200  $\mu\text{m}$  in size) were mounted in epoxy resin and polished down to expose their near equatorial sections. The analytical protocol for the BRGM is presented in Table S3 and the Plešovice zircon (Sláma *et al.*, 2008) used as quality control reference material yielded a concordia age of  $340 \pm 3$  Ma (MSWD = 1.5,  $n = 24$ ). The analytical protocol for the GeOHeLiS analytical Platform is presented in Table S4 and the Plešovice zircon (Sláma *et al.*, 2008) used as quality control reference material yielded a concordia age of  $337.6 \pm 2.0$  Ma (MSWD = 0.23,  $n = 15$ ). See Manzotti *et al.* (2016) for more details on the analytical protocol.

Two Al-rich metapelitic samples (*MCE339v* and *MCE338*) were investigated for their metamorphic evolutions through petrology and phase diagram calculations. Electron microprobe analysis has been performed at the University of Orléans on a CAMECA SX-FIVE. The P-T metamorphic conditions were obtained through calculations of pseudosection diagrams using Perple\_X 6.9.1. software (Connolly and Pettrini, 2002; Connolly, 2005; hpver62 database from Holland and Powell, 2011). The considered system was  $\text{MnO}-\text{Na}_2\text{O}-\text{CaO}-\text{K}_2\text{O}-\text{FeO}-\text{MgO}-\text{Al}_2\text{O}_3-\text{SiO}_2-\text{H}_2\text{O}$  (MnNCKFMASH). Solution models used in the calculations were garnet, biotite, white mica, staurolite, cordierite, chlorite, chloritoid and melt (White *et al.*, 2014) as well as plagioclase (Fuhrman and Lindsley,

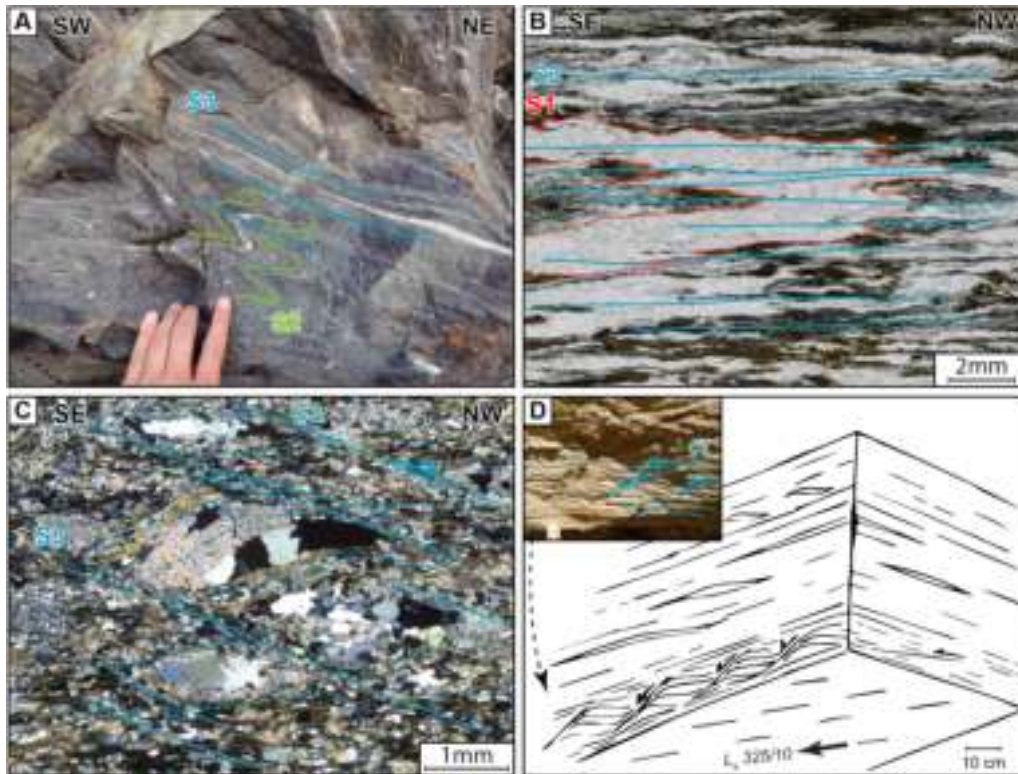


**Fig. 8.** Outcrop photographs and micro-photographs of the D<sub>3</sub> deformation. (A) Folding and transposition of the subvertical S<sub>2</sub> foliation by the flat laying S<sub>3</sub> foliation in the northern part of the *Le Rochail* block. (B) Folding and transposition of the relictual S<sub>1</sub> foliation by the flat laying S<sub>3</sub> foliation in the northern part of the *Le Rochail* block. (C) S<sub>3</sub>-C<sub>3</sub> structures showing top-to-the-NW kinematics from sample *MCE382b*. (D) Zoom of the photo E with top-to-the-NW kinematic indicators and schematic block diagram of the outcrop.

1988) and ilmenite (White *et al.*, 2000). Whole rock major element compositions (Tab. 2) were obtained using a PANalytical AxiosmAX X-Ray Fluorescence (XRF) Spectrometer at Lausanne University, Lausanne, Switzerland. The P-T conditions of biotite, muscovite and plagioclase equilibrium were estimated using the third model quality factor  $Q_{cmp}$  described in Duesterhoeft and Lanari (2020) in order to have a quantitative approach. This factor calculates the fitting between the mineral composition and the composition modelled and takes account of the relative analytical uncertainty of the extracted compositions. The comparison of mineral composition was restricted to MnO, MgO, FeO, SiO<sub>2</sub> and Al<sub>2</sub>O<sub>3</sub> contents for biotite, of Na<sub>2</sub>O, K<sub>2</sub>O, CaO, Al<sub>2</sub>O<sub>3</sub>, FeO, MgO and SiO<sub>2</sub> contents for muscovite, and of CaO, K<sub>2</sub>O, Na<sub>2</sub>O, SiO<sub>2</sub> and Al<sub>2</sub>O<sub>3</sub> contents for plagioclase.

#### 4.1 Gneissic mylonites (samples *MCE379* and *MCE382b*)

The sample *MCE379* is a gneiss from the volcano-sedimentary unit of the northern part of the Cortical Pelvoux where the main planar fabric is a composite S<sub>1-3</sub> foliation (Fig. 4A). It is composed of Qtz + Kfs + Bt with rare garnet and muscovite occurrences and few late white micas (Fig. 10A). It is structured by D<sub>1</sub> shear planes oriented N120°E/30NW, kinematic is not clear because of D<sub>3</sub> superimposition. Quartz

ribbons show undulose extinction and Grain Boundary Migration recrystallization (GBM; Stipp *et al.*, 2002). Monazite is located either in the quartzo-feldspathic matrix (Fig. 10B) or as an undeformed inclusion in biotite marking the S<sub>1</sub> foliation (Figs. 10C and 10D). Monazite grains do not show any zonation in BSE images (Fig. S1) and have U, Pb and Th contents ranging between 1322–3462 ppm, 869–2110 ppm and 22 326–72 038 ppm, respectively, with Th/U ratios between 8.1 and 27.8 (Tab. S1). Twenty-nine analyses were performed on 26 monazite grains within the matrix. Except two discordant analyses, all analyses yield a concordant date at  $334.8 \pm 3.2$  Ma ( $n = 27$ ;  $MSWD_{(C+E)} = 1.3$ ) (Fig. 11A).

Sample *MCE382b* is a gneiss coming from the same area as sample *MCE379* (Fig. 2). It is composed of Qtz + Kfs + Bt + Grt + late Ms (Fig. 10E). In this sample, D<sub>3</sub> strain is higher than in sample *MCE379* and the D<sub>3</sub> mylonitic planar fabric is oriented N133°E;30NE with a L<sub>3</sub> stretching lineation trending N120°E. C-S structures and sigmoidal quartz aggregates indicate top-to-the-NW kinematics (Fig. 10E). Quartz crystals are stretched and form quartz-ribbons with undulose extinction and GBM recrystallization.

Fourteen monazite grains from sample *MCE382b* have been analyzed *in situ*, they do not show any zonation (Fig. S1) but display two habitus: monazite included in large biotite marking the S<sub>3</sub> foliation (group 1; Figs. 10G and 10H) and monazite located inside the quartzo-feldspathic matrix (group 2;

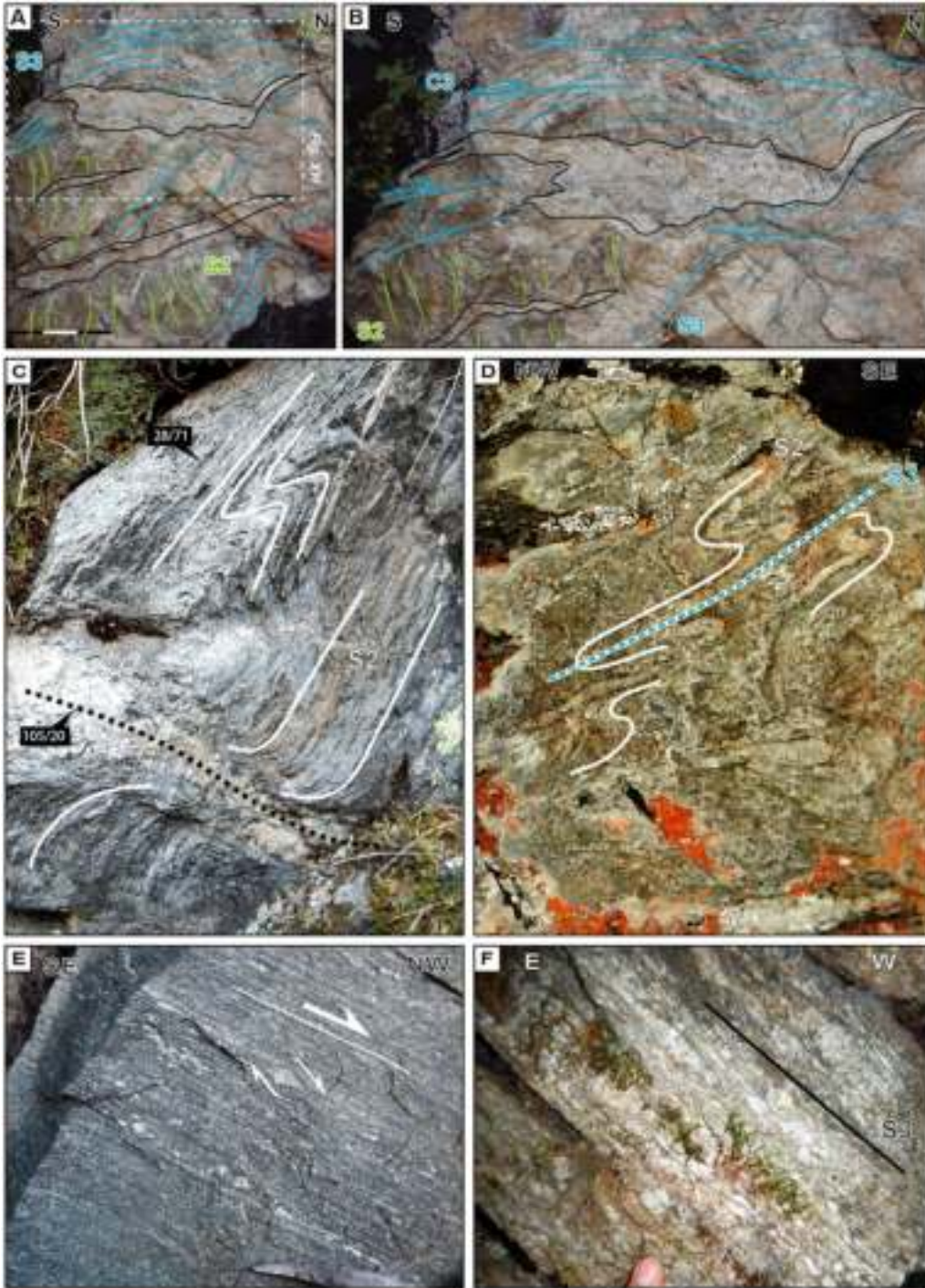


**Fig. 9.** Field pictures of D<sub>3</sub> deformation. (A and B) Low-angle S<sub>3</sub> reworking a steep S<sub>2</sub> foliation. Both foliations are melt-bearing and a pegmatitic leucosome parallels C<sub>3</sub> shear bands. The outcrop is located near the Gioberney mountain refuge. (C) Melt-bearing flat-lying D<sub>3</sub> shear zone cross-cutting the steep S<sub>2</sub> foliation. Outcrop photographs A, B C and D are located around the Gioberney mountain refuge, in the La Meige Block. (D) Vertical shortening of S<sub>2</sub> and development of axial planar S<sub>3</sub>. (E) Mylonitic S<sub>3</sub> with top-to-the-NW shearing at the base of the Cortical Pelvoux, near Villard-Notre-Dame village. (F) Moderately dipping migmatitic gneiss (MCE 330) showing a solid-state protomylonitic foliation S<sub>3</sub> developed during D<sub>3</sub> shearing and cooling.

**Table 1.** Summary of geographic location, rock types, and U-Pb geochronological results for samples analyzed in this study.

Sample	Rock type	GPS location	Mineral dated	U-Th-Pb age ( $\pm 2\sigma$ )
<b>Cortical Pelvoux</b>				
<i>MCE379</i>	Mylonitic gneiss	N45°1'23.49" E06°2'33.70"	Monazite	334.8 $\pm$ 3.2 Ma
<i>MCE382b</i>	Mylonitic Grt-gneiss	N45°1'2.61" E06°2'50.99"	Monazite	334.5 $\pm$ 3.4 Ma 306.0 $\pm$ 3.5 Ma
<i>MCE339v</i>	Grt-St-Ky-metapelite	N44°52'52.00" E05°59'17.34"	Monazite	346.6 $\pm$ 4.8 Ma 319.2 $\pm$ 6.1 Ma
<i>MCE338</i>	Sill-Grt-metapelite	N44°52'58.84" E06°0'49.10"	Monazite	333.2 $\pm$ 1.6 Ma
<i>MCE328</i>	Ky-St-metapelite	N44°47'12.12" E06°4'1.62"	Monazite	330.7 $\pm$ 3.1 Ma
<i>MCE330</i>	Roux migmatite	N44°47'29.86" E06°5'18.09"	Zircon	330.5 $\pm$ 3.1 Ma 590.6 $\pm$ 6.2 Ma
<b>Inner Pelvoux</b>				
<i>MCE314</i>	Peyre-Arguet Crd-migmatite	N44°50'6.69" E06°22'2.42"	Monazite	307.5 $\pm$ 1.9 Ma
<i>MCE313b</i>	Peyre-Arguet migmatite	N44°56'4.37" E06°12'55.58"	Zircon	451.4 $\pm$ 5.2 Ma
<i>MCE140b</i>	Etagés migmatite	N44°56'4.37" E06°12'55.58"	Zircon	297.8 $\pm$ 2.1 Ma 317.0 $\pm$ 3.6 Ma
<i>MCE304v2</i>	Peyre-Arguet metabasite	N44°50'15.34" E06°21'22.25"	Zircon	326.9 $\pm$ 9.1 Ma 471.3 $\pm$ 5.0 Ma

Fig. 10F). Monazite grains from the quartzo-feldspathic matrix (group 2) have U, Pb and Th contents between 740–1016 ppm, 1198–1796 ppm and 15 803–26 505 ppm, respectively, and Th/U ratios of 19.4–36.9 (Tab. S1). Monazite inclusions within large biotite marking the  $S_3$  foliation (group 1) have higher U contents (1241–1997 ppm), similar Pb and Th contents (1063–1478 ppm and 11 914–21 818 ppm), and lower Th/U ratios (6.1–16.4). Two ages can be identified (Fig. 11B), the oldest one is calculated from 7 monazite grains located in the matrix (group 2) that provide a concordant date at  $334.5 \pm 3.4$  Ma ( $MSWD_{(C+E)} = 0.88$ ). The second one is obtained from 4 grains included within large biotite (group 1) yielding a concordant date at  $306.0 \pm 3.5$  Ma ( $MSWD_{(C+E)} = 0.39$ ).

#### 4.2 Al-rich metapelites (samples MCE339v, MCE338 and MCE328)

Sample *MCE339v* is a micaschist composed of Qtz + Grt + Ky + St + Bt + Ms + Pl (Fig. 12A) sampled in the middle part of the Cortical Pelvoux (SW of Entraigues village, Fig. 2). It is structured by a pervasive  $D_2$  shear zone oriented N0°E;70E with a horizontal stretching lineation trending N0. Staurolite and kyanite are relictual and are strongly affected by the  $D_2$  shearing. An old foliation, probably  $S_1$ , is preserved in kyanite and garnet (Fig. 12B). Micas and quartz layers form sinistral sigmoidal wrapping around garnet porphyroblasts.

Garnet grains show a slight zonation (Fig. 13A) with a core composed of ca. 64% of almandine, 5% of pyrope, 18.5% of grossular and 12.5% of spessartine, and a rim composed of 74% of almandine, 12% of pyrope, 13% of grossular and 1% of spessartine (Tab. 3). Mineral compositions were modified by diffusion processes, as suggested by the smooth compositional zoning (Fig. 13A). Plagioclase is an oligoclase with  $Ab_{76}$ , and biotite presents a stable composition at  $X_{Fe} 0.57$  (Tab. 3). A phase equilibrium diagram was calculated for this sample with a  $H_2O$  content at 1.33 wt%, which corresponds to the saturation

of the sample at the solidus conditions as estimated from a T- $X_{H_2O}$  diagram (Fig. 13B). The obtained phase diagram defines a large stability field corresponding to the mineral assemblage of sample *MCE339v* (Qtz + Grt + Ky + St + Bt + Ms + Pl) with temperature and pressure conditions below 600 °C and 0.7 GPa, respectively (Fig. 13C). The phase diagram fails to reproduce the garnet core composition, perhaps due to diffusion process and modification of the initial composition of the garnet core. The  $Q_{cmp}$  factor of the plagioclase composition only slightly varies, and its maximal value is 99.8% of fitting with the reference composition (Fig. 13C). This highest  $Q_{cmp}$  value (Duesterhoeft and Lanari, 2020) indicates P-T conditions inferior to 650 °C and 0.6 GPa and is well expressed in the stability field of the mineral assemblage (Fig. 13C). The  $Q_{cmp}$  factor of the biotite reaches a value of 95% of fitting with the reference composition and indicates temperatures between 525 and 750 °C and pressure conditions between 0.4 and 0.7 GPa and only expressed in the stability field of the mineral assemblage at around 550 °C and 0.5 GPa (Fig. 13D). These results must be taken with caution due to potential diffusion processes that might have affected the mineral compositions and analytical uncertainties on the reference compositions.

Monazite grains from sample *MCE339v* do not show any zonation, however two populations are recognized: the first one (group 1) is composed of monazite grains not oriented within the  $S_2$  foliation and often included in quartz and sometimes in kyanite (Fig. 12B), displaying U, Pb and Th contents at 2985–6844 ppm, 1894–4304 ppm and 20 221–45 439 ppm, respectively, and medium Th/U ratios (5.1–7.6). The second population (group 2) is composed of monazite grains oriented parallel to the main  $S_2$  foliation in mica-rich layers (Fig. 12C), with higher U and Pb contents ranging at 7069–8247 ppm and 4006–4827 ppm, Th varying in the range 33 668–50 915 ppm. The Th/U ratios are in the range 4.8–6.7 (Tab. S1). Analyses performed on monazite grains from the

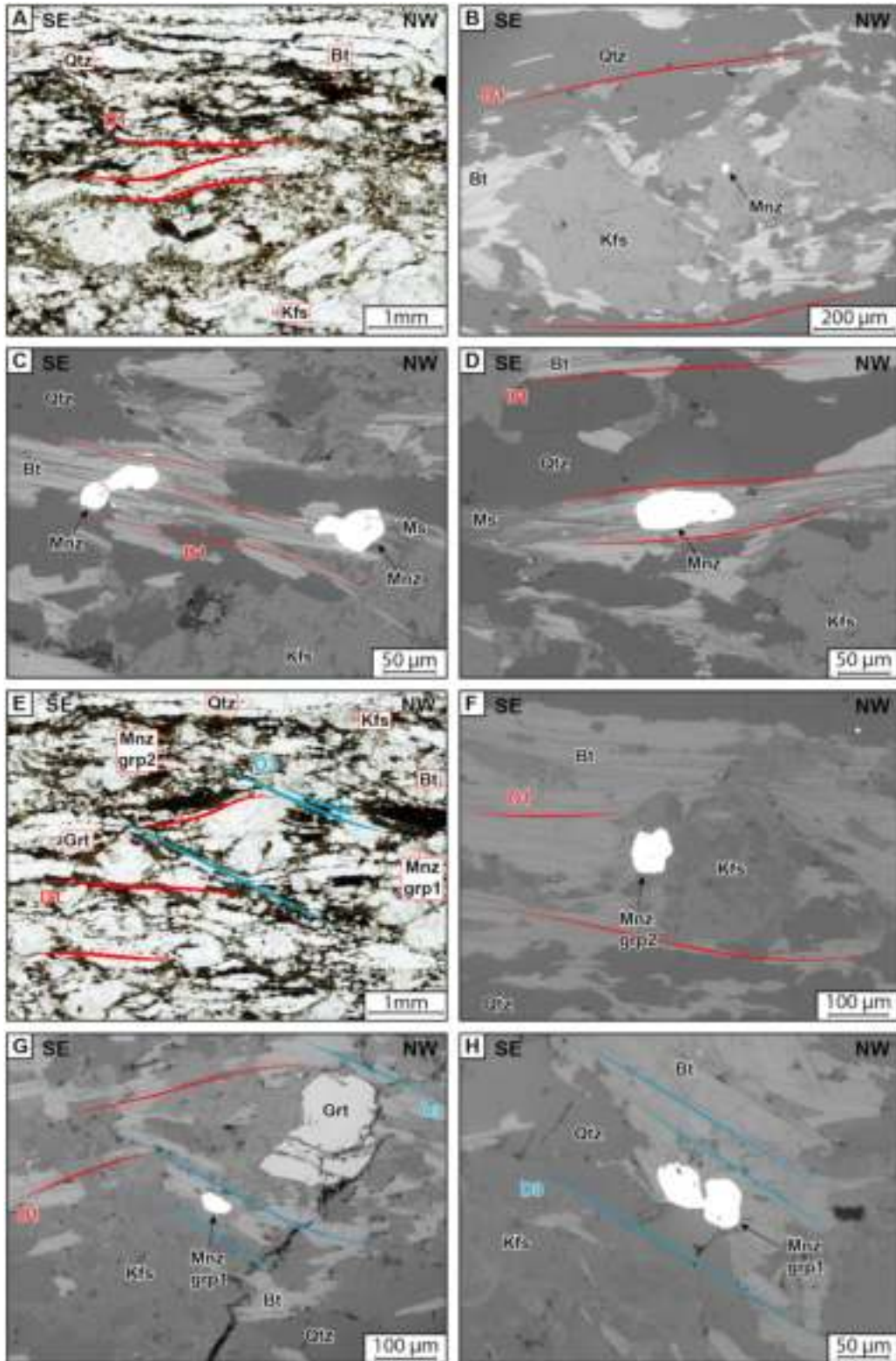


**Fig. 10.** Thin-sections photographs and BSE images showing structural and petrological relationships of samples *MCE379* and *MCE382b*. (A) Thin-section photograph of sample *MCE379* structured by  $D_1$  planar fabric. (B) BSE image of a monazite included in K-feldspar. (C and D) BSE images of monazite grains in mica marking the  $S_1$  foliation. (E) Thin-section photograph of sample *MCE382* structured by  $D_1$  planar fabric and  $D_3$  shear bands. (F) BSE image of a monazite included in K-feldspar. (G and H) BSE images of monazite grains in biotite marking the  $S_3$  foliation. Mineral abbreviations from Kretz (1983).

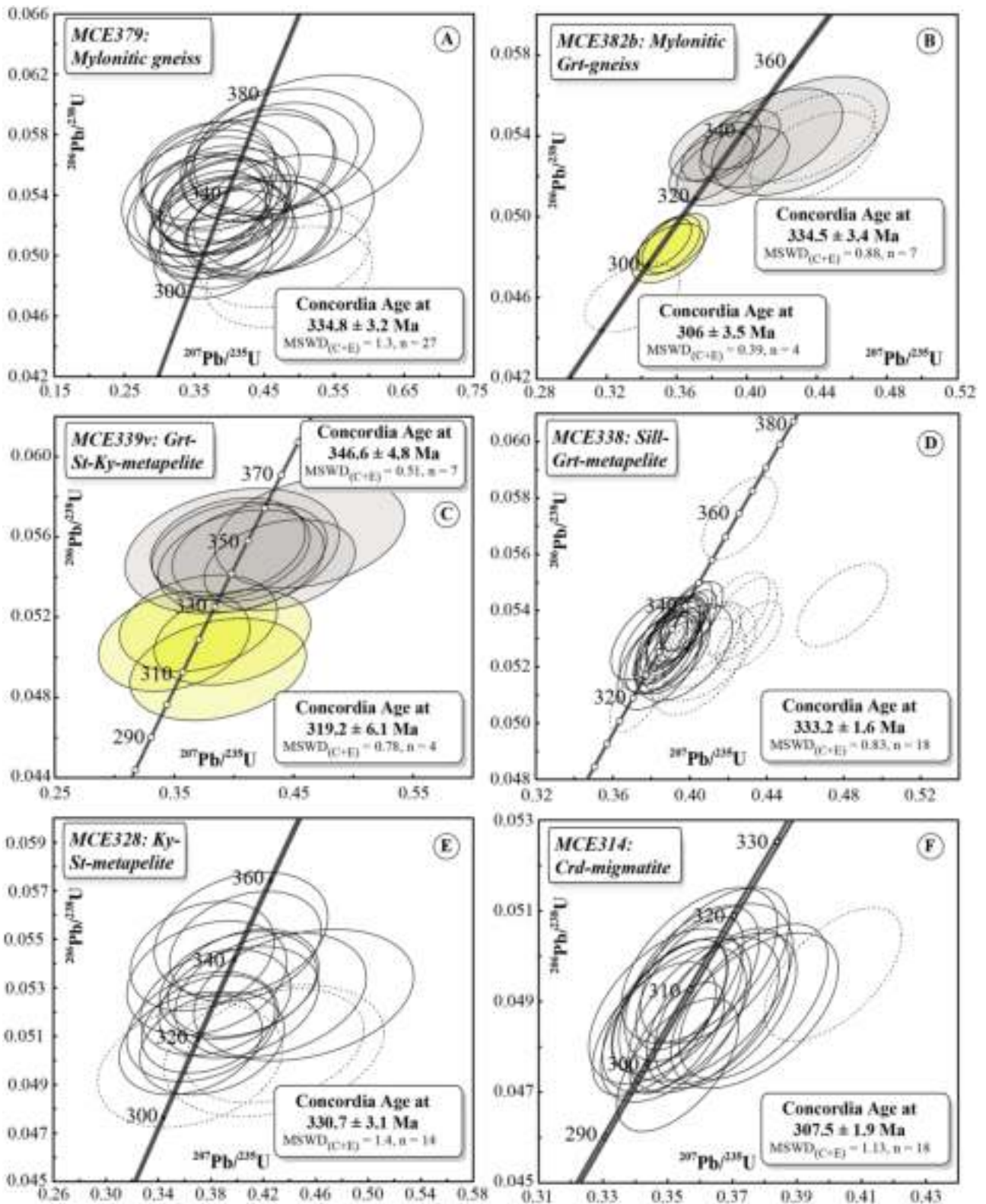


**Fig. 11.** Monazite U-Pb concordia diagrams obtained by LA-ICPMS. (A) MCE379; (B) MCE382b; (C) MCE339v; (D) MCE338; (E) MCE328; (F) MCE314. Error ellipses and uncertainties in ages are  $\pm 2\sigma$ . Dotted ellipses are not considered for the age calculation.

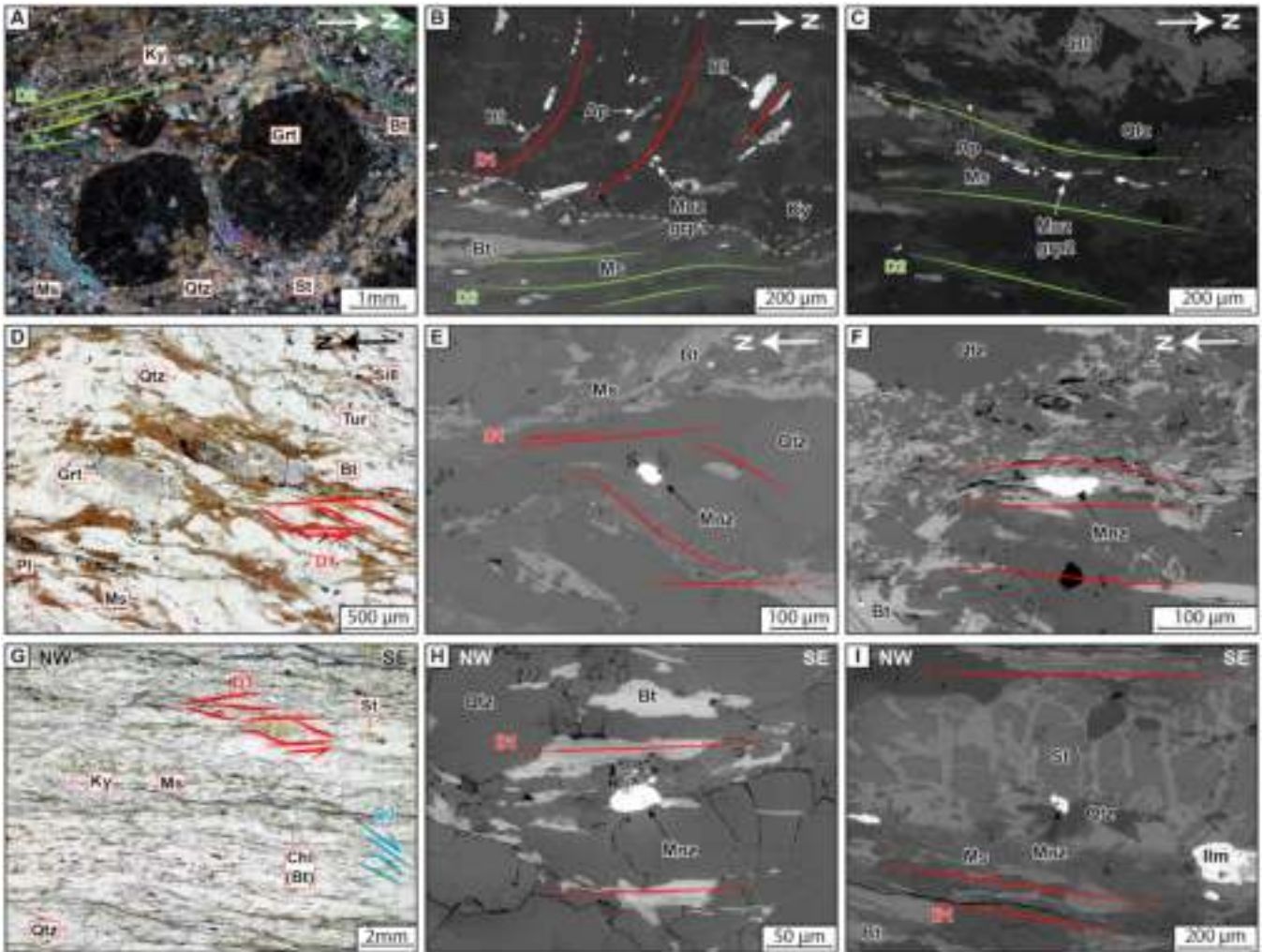


**Fig. 12.** Thin-sections photographs and BSE images showing structural and petrological relationships of samples *MCE339v*, *MCE338* and *MCE328*. (A) Thin-section photograph of sample *MCE339v* structured by  $D_2$  planar fabric. (B) BSE image of a monazite oriented parallel with the ancient  $S_1$  foliation preserved in kyanite (white dotted line). (C) BSE image of monazite grains in mica marking the  $S_2$  foliation. (D) Thin-section photograph of sample *MCE338* structured by  $D_1$  planar fabric showing elongated garnet grains parallel to the  $S_1$  foliation. (E) BSE image of a monazite included in quartz showing a sigmoidal shape. (F) BSE image of a monazite in micas marking the  $S_2$  foliation. (G) Thin-section photograph of sample *MCE328* structured by  $D_1$  planar fabric and  $D_3$  shear bands. (H) BSE image of a monazite elongated parallel to the  $S_1$  foliation included in quartz. (I) BSE image of a monazite staurolite and quartz.

first group yield a concordant date at  $346.6 \pm 4.8$  Ma ( $n = 7$ ;  $MSWD_{(C+E)} = 0.51$ ) (Fig. 11C), whereas analyses from the second group of monazite grains provide a concordant date at  $319.2 \pm 6.1$  Ma ( $n = 4$ ;  $MSWD_{(C+E)} = 0.78$ ).

Sample *MCE338* is a metapelite sampled in the middle of the Cortical Pelvoux (Fig. 2). It is composed of Qtz + Pl + Ms + Bt + Grt + Sill with scarce tourmaline (Fig. 12D). The main planar fabric is a  $S_1$  foliation showing numerous variscan sigmoidal and C-S structures reoriented by the alpine tectonics. Garnet grains are boudinaged by  $D_1$  with boudin necks filled by biotite, quartz and sillimanite (Fig. 12D). Fibrolitic sillimanite is localized in  $D_1$  structures and in  $D_1$  sigmoid tails, suggesting a syn- $D_1$  crystallization. A phase equilibrium diagram was calculated for this sample (Fig. 14).  $H_2O$  amount was defined at 1.47 wt%, which corresponds to the saturation of the sample at the solidus conditions of the mineral assemblage and was estimated from a T- $X_{H_2O}$  pseudosection

(Fig. 14B). Garnet grains show a slight zonation (Fig. 14A) with a core composed of ca. 71% of almandine, 12.5% of pyrope, 5.5% of grossular and 11% of spessartine, and a rim composed of 68.5% of almandine, 8.5% of pyrope, 4% of grossular and 19% of spessartine (Tab. 3). Plagioclase is homogeneous in composition with  $Ab_{75}$  and biotite presents a stable composition at  $X_{Fe}$  0.56 (Tab. 3). The resulting pseudosection (Figs. 11B and 11C) indicates a stability field with the mineral assemblage corresponding to the one observed in the sample (*i.e.*, Pl + Grt + Ms + Bt + Sill + Qtz). Due to its low proportion and variability, grossular was not used to constrain the P-T conditions. The almandine, pyrope and spessartine isopleths of the garnet core cross-cut at  $565 \pm 30$  °C and  $0.46 \pm 0.04$  GPa in the stability field of the observed mineral assemblage (Fig. 11B). Regarding the low volume of garnet in this sample (*i.e.*, inferior to 3 vol%), we did not calculate a new pseudosection removing the garnet core



bulk composition. Isopleths from the garnet rims cross-cuts at  $450 \pm 30$  °C and  $0.36 \pm 0.02$  GPa (Fig. 11B). The best  $Q_{\text{cmp}}$  values of the biotite and plagioclase do not perfectly fit with these P-T conditions, but their  $Q_{\text{cmp}}$  remains high at the P-T conditions defined by the garnet core composition (Figs. 14D and 14F). The best  $Q_{\text{cmp}}$  factor of the muscovite might indicate a higher-pressure stage around 0.7–0.8 GPa before the P-T conditions defined by the garnet core (Fig. 14E).

In the sample *MCE338*, monazite grains are included in quartz, in biotite and in muscovite-biotite layers (Figs. 12E and 12F). They are mainly parallel with the  $S_1$  foliation (Fig. 12F) and sometimes show syn- $D_1$  kinematic criteria (Fig. 12E). They do not show zonation on BSE images (Fig. S1). Twenty-eight analyses display U, Pb and Th contents ranging between 1486–5802 ppm, 786–3070 ppm and 7372–33 214 ppm, respectively, with constant Th/U ratios (4.2–6.1; Tab. SE1). By removing discordant data (ja8, ja11, ja15, ja20, ja24, ja27, ja28 and ja29; Tab. SE1), as well as the younger and older analyses (ja13 and ja5, respectively; Tab. SE1), the remaining data points provide a concordia date of  $333.2 \pm 1.6$  Ma ( $n = 18$ ;  $\text{MSWD}_{(\text{C+E})} = 0.83$ ) (Fig. 11D).

Sample *MCE328* is a micaschist from the southern part of the Cortical Pelvoux (Fig. 2). It is composed of quartz, muscovite, biotite, staurolite and kyanite (Fig. 12G). The main planar fabric of this sample is a composite  $S_{1-3}$  foliation oriented N160°E;25E with a subhorizontal  $L_3$  stretching lineation trending N160°E. The quartz and micas sigmoidal aggregates indicate a  $D_1$  top-to-the-NW sense of shear, while  $D_3$  shear bands indicate top-to-the-SE kinematics (Fig. 12G). Kyanite and staurolite, often surrounded by a white mica-corona, are deformed by the  $D_3$  shear bands. Biotites are commonly chloritized. Monazite grains are mainly located in the quartz-matrix or in biotite marking the  $S_1$  foliation and are typically oriented parallel to the  $S_1$  foliation (Fig. 12H). Some monazite grains also seem included in staurolite (Fig. 12I). They do not show chemical zoning (Fig. S1). The analyzed grains display U, Pb and Th contents ranging between 3761–8639 ppm, 2160–5277 ppm and 24 475–45 307 ppm, respectively, and constant Th/U ratios (5.2–7.1 except one data at 4.0; Tab. S1). As the whole, 17 analyses were performed, among them, 14 are concordant and yield a concordia date of  $330.7 \pm 3.1$  Ma ( $\text{MSWD}_{(\text{C+E})} = 1.4$ ) (Fig. 11E).

### 4.3 Migmatites (samples *MCE314*, *MCE330*, *MCE140b* and *MCE313b*)

The cordierite bearing migmatite *MCE314* has been sampled in the Inner Pelvoux Massif (Fig. 2). It is composed of quartz, K-feldspar, muscovite, chloritized biotite and pinitized cordierite. This sample exhibits a highly dipping and N140°E striking  $S_2$  foliation defined by quartz aggregates and phyllosilicates. Subsidiary deformation is rare, and  $S_2$  foliation is mainly a suprasolidus planar fabric. The alpine tectonics induced a low-grade retrogression as shown by chlorite around biotites, and sericite around K-feldspar. Unfortunately, because of alpine retrogression and strong pseudomorphosis of cordierite, pseudosection calculation was not possible. One may consider that cordierite-bearing migmatites are generally formed under low-pressure and high temperature conditions at ca. 0.4–0.6 GPa; 750–850 °C (Barbey *et al.*, 1999; Kalt *et al.*, 1999).

Monazite grains, located within the quartzo-feldspathic matrix, are not zoned and display heterogeneous U and Th contents (3437–10 171 ppm and 5909–86 534 ppm, respectively), relatively constant Pb content (1210–5516 ppm), and heterogeneous Th/U ratios (1.3–20.2) (Tab. S1). Despite this chemical heterogeneity, all analyses are concordant or sub-concordant (except jb7; Tab. S1), and yield a concordia date of  $307.5 \pm 1.9$  Ma ( $n = 18$ ;  $\text{MSWD}_{(\text{C+E})} = 1.4$ ) (Fig. 12F).

The Roux migmatite (*MCE330*), located in the Cortical Pelvoux, is a migmatitic gneiss developed at the base of the VSU (Figs. 2 and 4B). It is composed of quartz + K-feldspar + plagioclase + Biotite + Muscovite and is the equivalent of the Allemont migmatites from the SW Belledonne area (Fréville *et al.*, 2018). The *MCE330* migmatite shows a N110°E40 solid-state protomylonitic foliation that erased syn-melting fabrics (Fig. 9F). The preferred orientation of mica and quartz-feldspar aggregates defines S-C fabrics that we attribute to  $D_3$ . The CL images of the analysed zircon grains show inherited cores with a typical magmatic concentric oscillatory zoning and metamorphic rims (Fig. S1). Zircon cores and rims have similar U and Pb contents ranging between 247–2605 ppm and 12–140 ppm, respectively (Tab. S1). Thirty analyses have been performed on 30 zircon grains (Fig. 15A). In the Tera-Wasserburg diagram, analyses mainly cluster into two groups. The first one, includes 13 concordant analyses on zircon cores, indicate a late Neoproterozoic age of crystallization. Among them, 9 analyses yield a concordant date at  $590.6 \pm 6.2$  Ma ( $\text{MSWD}_{(\text{C+E})} = 0.95$ ). Two zircon cores show concordant and sub-concordant dates at ca. 1700 Ma and 1800 Ma (Fig. 15A), and two single analyses yield concordant dates at ca. 405 and 380 Ma. The second cluster includes 12 analyses performed on zircon rims and yields a concordia date at  $330.5 \pm 3.1$  Ma ( $\text{MSWD}_{(\text{C+E})} = 0.92$ ) (Fig. 15A).

The Etages migmatite (*MCE140b*), located in the Inner Pelvoux, forms the country rock of the Etages granite (Figs. 2 and 4A). Composed of chloritized biotite, feldspars and quartz this rock shows a slight  $C_2$  orientation, and it was also superimposed by a low-temperature alpine deformation (Fig. 4A). Euhedral zircon crystals with elongated shapes present oscillatory zonings in CL (Fig. S1). Twenty-eight zircon grains were analysed and they form two age groups (Fig. 15B). The first one is composed of four analyses forming a concordant cluster with low U, Pb and Th contents and Th/U ratios ranging from 0.08 to 0.5 (Tab. S1), that yields a concordant date at  $317 \pm 3.6$  Ma ( $\text{MSWD}_{(\text{C+E})} = 0.38$ ) (Fig. 15B). The second group is composed of 22 analyses with higher U, Pb and Th contents than the first group, but with similar Th/U ratios ranging from 0.06 to 0.5 (Tab. S1). Among this group, numerous analyses show lead loss (Fig. 15B) but ten analyses define a concordant date at  $297.8 \pm 2.1$  Ma ( $\text{MSWD}_{(\text{C+E})} = 0.66$ ) (Fig. 15B). In addition, one analysis shows a concordant date at ca. 460 Ma.

The Peyre-Arguet cordierite-bearing migmatite (*MCE313b*) displays a  $C_2$  foliation along which the cordierite grains are aligned. Zircon grains display patchy and oscillatory zoning (Fig. S1). Nineteen grains have been analysed and they broadly scatter along the Concordia between 650 and 280 Ma. The most abundant age population is defined by 12 analyses ranging from 481 Ma to 419 Ma with low U (292–1043 ppm) and Pb (19–66 ppm) contents (Tab. SE1). Among this group,

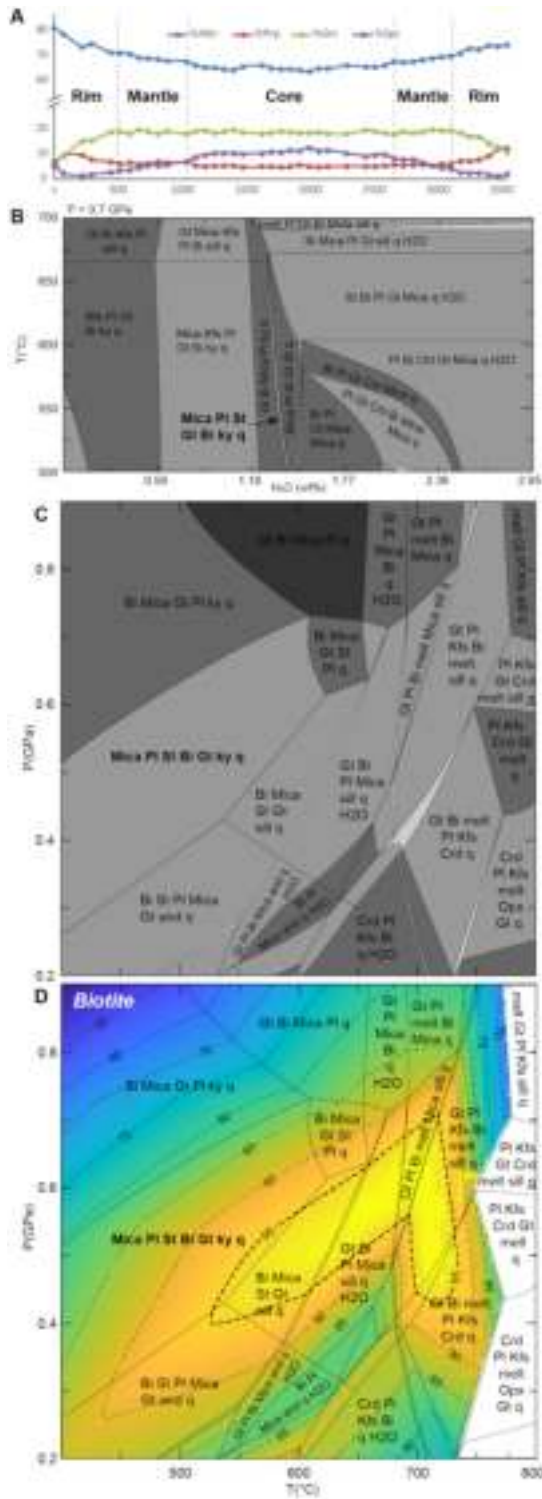


**Fig. 13.** Thermobarometric modelling of metapelitic sample *MCE339v* located in the Cortical Pelvoux. (A) Chemical profile of a garnet. (B) T-XH<sub>2</sub>O diagram calculated with a pressure of 0.7 GPa, the mineral assemblage of the sample indicates a H<sub>2</sub>O content of 1.33 wt%. (C) Pseudosection calculated in the MnNCKFMASH system. (D) Modelling of the Q<sub>cmp</sub> factor of the mineral composition of biotite based on MgO, FeO, MnO, Al<sub>2</sub>O<sub>3</sub> and SiO<sub>2</sub> contents (Tab. S2). Bi: Biotite; Mu: muscovite; Crd: Cordierite; Kfs: K-feldspar; Pl: Plagioclase; Gt: Garnet; and: Andalousite; ky: Kyanite; sill: Sillimanite; Opx: Orthopyroxene; q: Quartz; melt: silicate liquid.

7 analyses yield a concordant date of  $451.4 \pm 5.2$  Ma ( $\text{MSWD}_{(C+E)} = 0.66$ ) (Fig. 15C).

#### 4.4 Peyre-Arguet garnet amphibolite (sample MCE304v2)

The Peyre-Arguet meta-mafic (*MCE304v2*) is a garnet-bearing amphibolite from the Inner Pelvoux (Fig. 2) that consists of an amphibole, quartz, plagioclase and garnet assemblage that recorded D<sub>2</sub> deformation. Relics of clinopyroxene have been described by Barfety *et al.* (1982) and Jacob *et al.* (2022). Rutile grains are included within garnet and are replaced by ilmenite in the matrix. Garnet grains are surrounded by plagioclase-amphibole coronas. CL images of zircon included in garnet cores show cores with concentric oscillatory zoning surrounded by near homogeneous rims (Fig. S1). Zircon cores have high U (102–1349 ppm) and Pb (6.8–89.6 ppm) contents compared to rims (U: 3–72 ppm; Pb: 0.1–3.3 ppm) (Tab. SE1). Twenty-nine analyses have been performed on 29 zircon grains that define two clusters (Fig. 13D). The first one, composed of 12 concordant analyses from zircon cores, yields a concordant date at  $471.3 \pm 5$  Ma ( $\text{MSWD}_{(C+E)} = 1.06$ ;  $n = 11$ ) (Fig. 15D). The second cluster is formed by 11 analyses performed on zircon rims that define a lower intercept at  $329.6 \pm 9.2$  Ma ( $\text{MSWD} = 0.85$ ). Among them, 8 analyses yield a concordant date at  $326.9 \pm 9.1$  Ma ( $\text{MSWD} = 0.85$ ) (Fig. 15D). Several analyses show concordant dates at ca. 379, 385, 409 and 432 Ma, which probably reflect a mixture between an old core (~ 470 Ma) and a younger rim (~ 327 Ma) and are probably therefore without geological meaning.

## 5 Discussion

### 5.1 Pre-Variscan history

Inherited dates at  $451.4 \pm 5.2$  Ma and  $460 \pm 10$  Ma were obtained from magmatic zircon grains of the Peyre-Arguet and Etages migmatites (samples *MCE313b* and *MCE140b*; Fig. 15; Tab. S1). This Ordovician record is interpreted as the emplacement age of felsic laccoliths, *i.e.*, the protolith of orthogneisses. Numerous orthogneiss derived from Ordovician protoliths are well documented in the entire Variscan belt (*e.g.*, Melleton *et al.*, 2010; Lardeaux *et al.*, 2014) as within the ECMs (*e.g.*, Schaltegger, 1993; Sergeev and Steiger, 1993; Bussy and Von Raumer, 1994; Bussy *et al.*, 2011; Bussien Grosjean *et al.*, 2017). Even though a continental magmatic arc setting is sometimes suggested, presently, the preferred interpretation for the Ordovician magmatism is rather a rifting episode related to the opening of the Variscan oceans (*e.g.*, Von Raumer *et al.*, 1999, Vanderhaeghe *et al.*, 2020).

Similarly, the magmatic zircon cores from the Peyre-Arguet amphibolite (sample *MCE304v2*) display an inherited date of  $471.3 \pm 5$  Ma that likely represents the intrusion age of a mafic protolith during the Ordovician crustal thinning, in agreement with inheritance recorded in other metabasites from the ECMs (Paquette *et al.*, 1989; Oberli *et al.*, 1994; Rubatto *et al.*, 2001; Bussy *et al.*, 2011; Jacob *et al.*, 2021, 2022; Vanardois *et al.*, 2022).

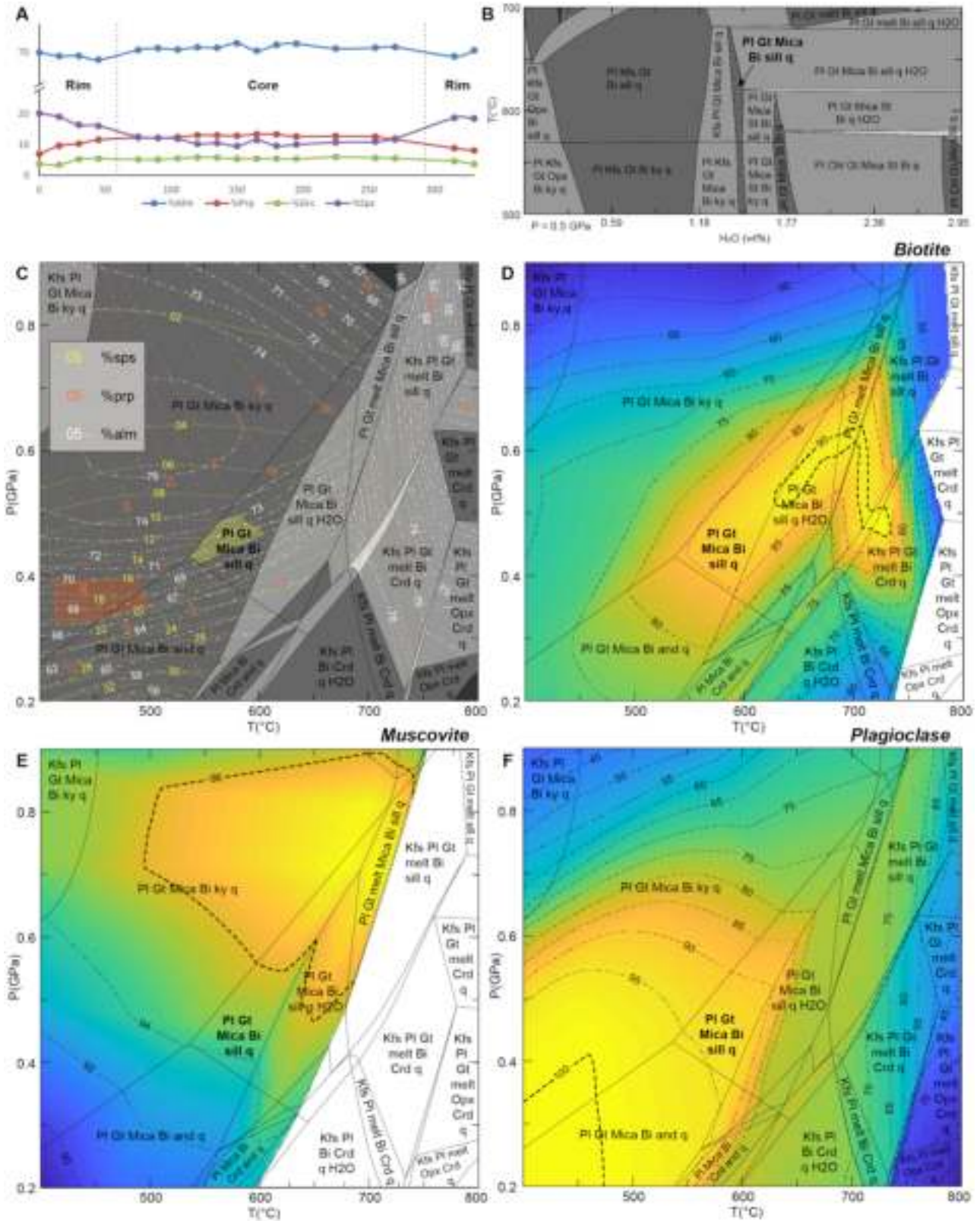


**Fig. 14.** Thermobarometric modelling of metapelite sample *MCE338* located in the Cortical Pelvoux. (A) Chemical profile of a garnet. (B) T-XH<sub>2</sub>O diagram calculated with a pressure of 0.5 GPa, the mineral assemblage of the sample indicates a H<sub>2</sub>O content of 1.47 wt%. (C) Pseudosection calculated in the MnNCKFMASH system. Modelling of the Qcmap factor of the mineral composition of (D) biotite based on MgO, FeO, MnO, Al<sub>2</sub>O<sub>3</sub> and SiO<sub>2</sub> contents, (E) muscovite based on Na<sub>2</sub>O, K<sub>2</sub>O, CaO, Al<sub>2</sub>O<sub>3</sub>, FeO, MgO and SiO<sub>2</sub> contents, and (F) plagioclase based on K<sub>2</sub>O, Na<sub>2</sub>O, CaO, Al<sub>2</sub>O<sub>3</sub> and SiO<sub>2</sub> contents (Tab. S2). Bi: Biotite; Mu: muscovite; Crd: Cordierite; Kfs: K-feldspar; Pl: Plagioclase; Gt: Garnet; and: Andalousite; ky: Kyanite; sill: Sillimanite; Opx: Orthopyroxene; q: Quartz; melt: silicate liquid.

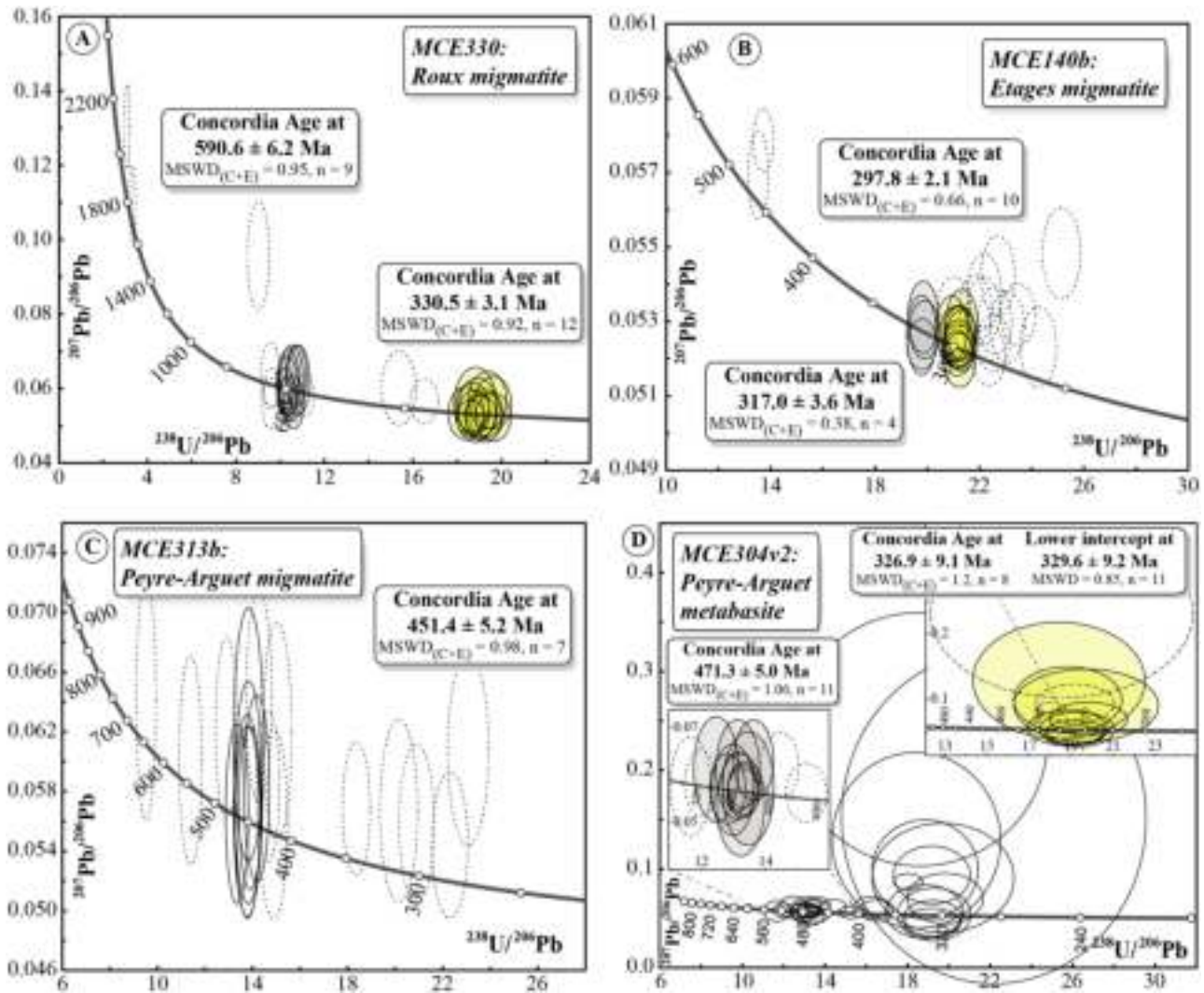


**Fig. 15.** Zircon U-Pb Tera–Wasserburg diagrams obtained by LA-ICPMS. (A) *MCE330*; (B) *MCE140b*; (C) *MCE313b*; (D) *MCE304v2*. Error ellipses and uncertainties in ages are  $\pm 2\sigma$ . Dotted ellipses are not considered for the age calculation.

Older detrital and inherited zircon ages from pre-Neoproterozoic to Cambrian were also obtained (Fig. 15). Lack of Mesoproterozoic dates ( $>1500$  Ma; Fig. 15A) point to a Gondwanian origin, *i.e.*, the West African Craton (*e.g.*, Melleton *et al.*, 2010; Linnemann *et al.*, 2014; Gärtner *et al.*, 2017), and NE Africa-Arabia, Baltica and Amazonia (Stephan *et al.*, 2019) as possible source regions. In the Cortical Pelvoux, the Roux migmatite (*MCE330*) did not record any Ordovician inheritance, but magmatic zircon cores rather indicate a Neoproterozoic magmatism at  $590.6 \pm 6.2$  Ma (Fig. 13A). The Roux migmatite did not originate from the partial melting of an Ordovician intrusive protolith but from that of a metasedimentary protolith probably related to Pan-African (750–600 Ma) or Cadomian (590–540 Ma) orogeneses (Linnemann *et al.*, 2014). Similar metasedimentary rocks in the SW Belledonne display inherited zircons at ca. 590 Ma (Fréville *et al.*, 2018). These Pan-African and Cadomian inherited zircon ages are common in the South-Western Variscan belt (*e.g.*, Roger *et al.*, 2004; Melleton *et al.*, 2010; Schnapperelle *et al.*, 2020) with a possible source region linked

to the north-eastern Gondwana margin (Linnemann *et al.*, 2014; Couzinié *et al.*, 2014; Von Raumer *et al.*, 2015; Chelle-Michou *et al.*, 2017).

## 5.2 Carboniferous crustal thickening ( $D_1$ deformation)

The mineral assemblage Qtz + Bt + Ms + Pl + Grt + Ky + St from sample *MCE339v* defines a large stability field with P-T conditions lower than 0.75 GPa and 625 °C (Fig. 13C). A set of old monazite grains, some being included in kyanite, yield a concordant date at  $346.6 \pm 4.8$  Ma that gives a time constraint for prograde metamorphism (Fig. 16b). In the sample *MCE338*, the main assemblage Qtz + Ms + Bt + Pl + Grt + Sill (Fig. 12D) gives P-T conditions between 550–700 °C and 0.35–0.80 GPa (Fig. 16a). The highest Qcmp factors for muscovite and biotite give a P-T refinement at ca. 0.6 GPa and 650 °C (Fig. 16a). Garnet grains are also a part of the mineral assemblage and mark the same planar fabric than micas (Fig. 12D), but their core compositions are best modelled at

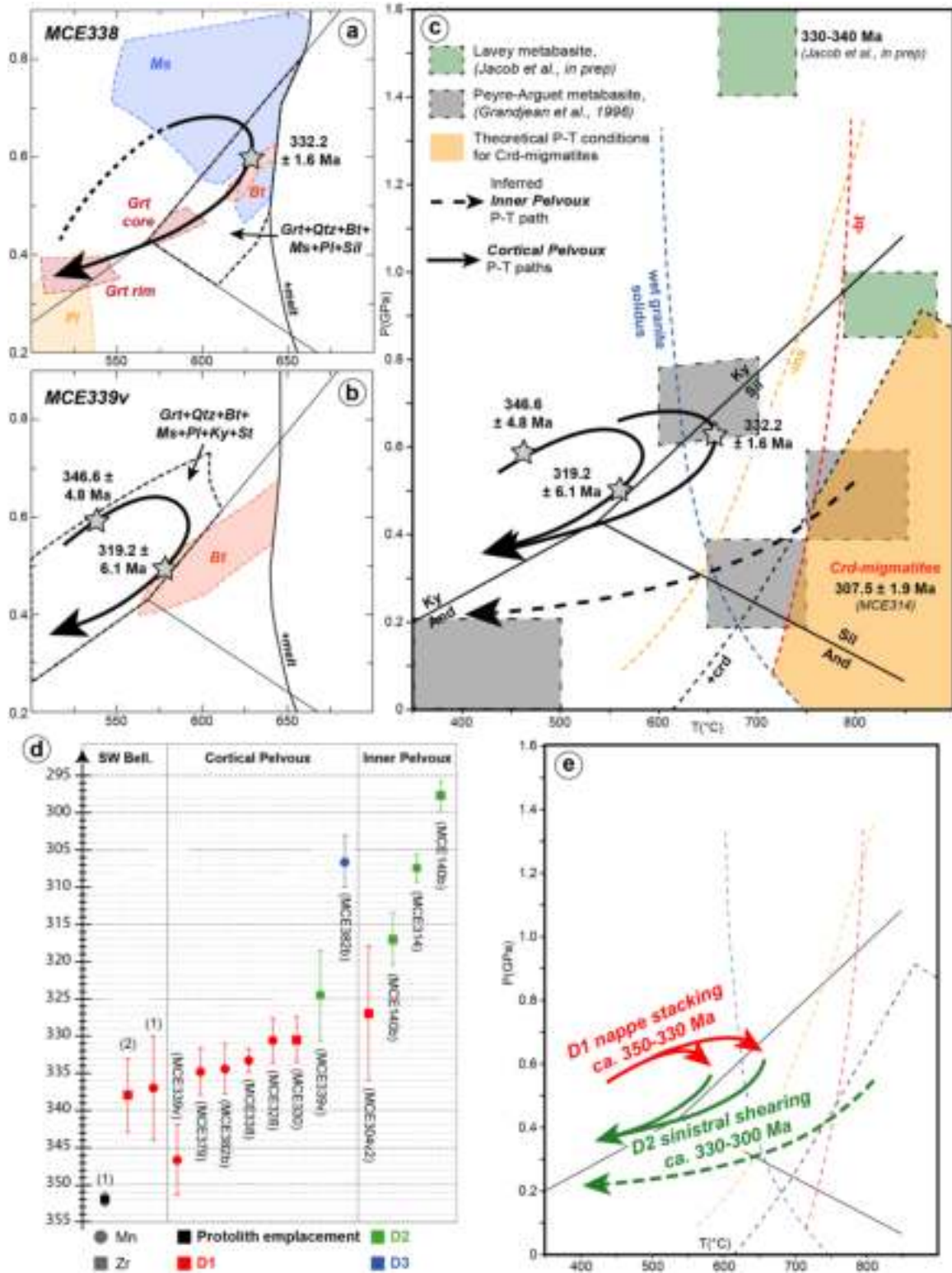


**Fig. 16.** Geochronological and tectono-metamorphic interpretations for the Pelvoux Massif. (a) P-T-t path of sample MCE338 inferred from the mineral assemblage and mineral compositions and from textural features of monazite. (b) P-T-t path of sample MCE339v inferred from the mineral assemblage and biotite composition and from textural features of monazite. (c) P-T-t conditions from the Pelvoux Massif. P-T-t paths of the Cortical Pelvoux are from this study. P-T data from metabasites of the Inner Pelvoux are from [Jacob \*et al.\* \(2022\)](#) and [Grandjean \*et al.\* \(1996\)](#). P-T conditions of Crd-migmatites are theoretical and age corresponds to monazite age of sample MCE314 from this study. (d) Geochronological results constraining the ages of D<sub>1</sub>, D<sub>2</sub> and D<sub>3</sub> from this study, ([Fréville \*et al.\*, 2018](#); [Fréville, 2016](#)). (e) Inferred tectono-metamorphic evolutions of the Cortical and Inner Pelvoux.

**Table 2.** Bulk-chemical composition in weight percent oxides for samples *MCE339v* and *MCE338*.

Oxyde (wt%)	SiO <sub>2</sub>	Al <sub>2</sub> O <sub>3</sub>	FeO	MgO	CaO	Na <sub>2</sub> O	K <sub>2</sub> O	TiO <sub>2</sub>	MnO	P <sub>2</sub> O <sub>5</sub>	Cr <sub>2</sub> O <sub>3</sub>	NiO	LOI	total
<i>MCE339v</i>	67.30	16.00	5.95	2.26	1.01	2.09	3.18	0.75	0.07	0.16	0.01	0.00	2.15	100.93
<i>MCE338</i>	59.70	19.00	7.32	3.26	1.09	2.07	3.82	0.93	0.11	0.12	0.02	0.00	2.95	100.39

lower-grade conditions (0.45 GPa and 575 °C; Fig. 14c). Garnet core shows a perfect homogeneous composition (Fig. 14A) that might be the result of diffusion process, which could explain the lower grade metamorphic conditions defined by the garnet core composition. Garnet rim composition yields P-T conditions at 0.35 GPa and 450 °C (Fig. 14c). The mineral composition modelling highlights a retrograde P-T path from the peak of metamorphism at ca. 0.6 GPa and 650 °C to the end of the retrograde path at 0.35 GPa and 450 °C (Fig. 16a). In the corresponding sample *MCE338*, monazite grains are often localized within biotite-muscovite layers (Fig. 12F) and yield a concordant date of  $332.2 \pm 1.6$  Ma (Fig. 11D), which is therefore interpreted as the age of the peak of M<sub>1</sub> metamorphism. These two samples present near similar P-T paths (Fig. 16c) with metamorphic conditions slightly higher in the sample *MCE338*, which is consistent with its deeper position into the crust (see Fig. 4B).

In sample *MCE339v*, the relictual S<sub>1</sub> foliation preserved in garnet and kyanite is dated by monazite at  $346.6 \pm 4.8$  Ma. Similarly, the S<sub>1</sub> foliation in the sample *MCE338* is defined by the alignment of micas and by the orientation of monazite and is dated at  $332.2 \pm 1.6$  Ma. Similar ages are obtained in samples *MCE379*, *MCE382b* and *MCE328* with a main S<sub>1</sub> foliation with syn-kinematic monazite grains (Figs. 10–12). These results indicate that a D<sub>1</sub> deformation was active at ca. 345–330 Ma (Fig. 16d).

A similar D<sub>1</sub>/M<sub>1</sub> event is documented in the SW Belledonne area with the well-preserved low angle S<sub>1</sub>, holding a E-W trending L<sub>1</sub> stretching lineation, interpreted as due to an eastward nappe stacking event responsible for crustal thickening coeval with the barrovian metamorphism (M<sub>1</sub>) (Fernandez *et al.*, 2002; Guillot *et al.*, 2009; Guillot and Ménot, 2009; Fréville *et al.*, 2018). In SW Belledonne Massif, the peak of M<sub>1</sub> metamorphism is dated on monazite (LA-ICP-MS) and zircon (SIMS) at around  $337 \pm 7$  Ma and  $338 \pm 5$  Ma respectively (Fig. 16d; Fréville *et al.*, 2018). The D<sub>1</sub>/M<sub>1</sub> barrovian evolution culminated with the partial melting as observed at the bottom of the VSU in the Cortical Pelvoux and SW Belledonne (Gidon *et al.*, 1980; Barfety *et al.*, 1988; Guillot *et al.*, 2009; Fréville *et al.*, 2018; this study) as exemplified by the “Roux migmatite” that yields a similar concordant age at  $330 \pm 3$  Ma (Fig. 15A) obtained on metamorphic rims of zircons (sample *MCE330* in this study).

The deposition age of the SW Belledonne VSU is dated at  $352 \pm 1$  Ma from a plagioclase-rich leucocratic sill (Fréville *et al.*, 2018). Based on the lithological similarities of these volcano-sedimentary rocks in SW Belledonne and Cortical Pelvoux, we propose that the volcano-sedimentary rocks of the Cortical Pelvoux deposited during the late-Devonian early-Carboniferous rifting and therefore predated the D<sub>1</sub> crustal thickening.

Retrogressed eclogites and HP granulites are well documented in others ECMs (*e.g.*, Albrecht *et al.*, 1991;

Von Raumer and Bussy, 2004; Ferrando *et al.*, 2008; Jouffray *et al.*, 2020; Jacob *et al.*, 2021; Vanardois *et al.*, 2022) and yield zircon and rutile ages at ca. 340–330 Ma (Rubatto *et al.*, 2010; Vanardois *et al.*, 2022). Recently, M<sub>1</sub> high-pressure peak condition recorded within retrograded eclogites of the NE Belledonne and Inner Pelvoux was constrained at ca. 340–330 Ma (Jacob *et al.*, 2021, 2022). In the Inner Pelvoux, the Peyre-Arguet mafic HP granulite (Barfety *et al.*, 1982) recorded a metamorphic age at  $326.9 \pm 9.1$  Ma (Fig. 15D), confirming that a D<sub>1</sub>/M<sub>1</sub> crustal thickening event at 350–330 Ma is recorded in both the Pelvoux and Belledonne Massifs (Fig. 16e). Consistently, the sub-horizontal magmatic foliation we recognized in the Rochail granite and dated at  $343 \pm 11$  Ma age (Guerrot and Debon, 2000) is interpreted as a S<sub>1</sub> foliation that resulted from crustal thickening.

### 5.3 Sinistral transpression and longitudinal flow (D<sub>2</sub> and D<sub>3</sub> deformations)

In the Cortical Pelvoux, the D<sub>2</sub> tectono-metamorphic event corresponds to a NW-SE shortening responsible for folding of the S<sub>1</sub> and formation of the N30°E striking S<sub>2</sub> foliation, also documented in the SW Belledonne (Fréville *et al.*, 2018), in the course of D<sub>1</sub> contraction. In sample *MCE339v*, from the central part of the Cortical Pelvoux, the S<sub>2</sub> foliation is defined by the preferential alignment of biotite for which the highest Q<sub>comp</sub> factor indicates temperature conditions above 525 °C and allows us to refine the P-T condition of biotite-bearing S<sub>2</sub> foliation at around 0.5 GPa and 550 °C near the kyanite-sillimanite transition (Fig. 13D). Monazite grains included in the biotite-layers (Fig. 12C) yield an age at  $319.2 \pm 6.1$  Ma (Fig. 11C) providing a time constraint for D<sub>2</sub> transpression (Fig. 16b).

In the Inner Pelvoux, D<sub>2</sub> structures are ubiquitous with the development of penetrative and steeply dipping planar surfaces, such as the S<sub>2</sub> foliation, and C<sub>2</sub>-C<sub>2</sub>' sinistral shear zones, and weakly plunging lineations formed under sinistral strike-slip regime (Fig. 17A). The syn-D<sub>2</sub> cordierite-bearing migmatite *MCE314* shows U-Th-Pb data obtained on monazite grains that form a cluster with an intercept at  $307.5 \pm 1.9$  Ma (Fig. 11F). It suggests that the partially molten crust was under high temperature and low-pressure conditions at ca. 308 Ma (Fig. 16c), giving another time constraint for the D<sub>2</sub> deformation. In the stages migmatite (*MCE140b*), four zircon grains yield a concordant date at  $317 \pm 4$  Ma (Fig. 13B) that we also relate to the D<sub>2</sub> transpression. The Etages migmatite *MCE140b* also gives a concordant date at  $297.8 \pm 2.1$  Ma, like the age of the Etages and the Bérarde-Promontoire syn-D<sub>2</sub> plutons (this study; Strzeczynski *et al.*, 2005) dated at ca. 303–299 Ma (Fréville, 2016). Hence, we propose that the timing of the D<sub>2</sub> transpression ranged from at least ca. 320 Ma to 298 Ma (Fig. 16d), but it might have started as early as 330 Ma

**Table 3.** Representative chemical compositions of minerals used for themobarometric calculation.

	Garnet		Biotite		Muscovite	Plagioclase		
		MCE338	MCE339v	MCE338	MCE338	MCE338		
	Rim	Core	Rim					
MCE339v								
Core								
<i>Oxydes (wt%)</i>								
SiO <sub>2</sub>	36.39	36.71	36.38	36.54	34.19	35.05	46.27	61.19
Al <sub>2</sub> O <sub>3</sub>	20.34	20.44	20.48	20.16	19.23	18.45	36.41	23.14
TiO <sub>2</sub>	0.19	0.05	0.03	0.01	1.66	1.47	0.34	
FeO	29.56	33.90	31.96	30.09	20.16	20.48	1.33	
MgO	1.27	2.31	3.14	2.02	8.63	9.10	0.69	
MnO	4.57	0.86	4.78	8.13	0.05	0.05	0.02	
CaO	6.62	5.14	1.93	1.31	0.00	0.02	0.03	4.83
Na <sub>2</sub> O					0.11	0.18	1.31	8.61
K <sub>2</sub> O					8.51	8.99	9.62	0.11
<i>Total</i>	<i>98.94</i>	<i>99.41</i>	<i>98.70</i>	<i>98.26</i>	<i>92.54</i>	<i>93.79</i>	<i>96.02</i>	<i>97.88</i>
<i>Mol cations</i>								
Si	2.97	2.97	2.97	3.02	2.68	2.72	3.05	2.79
Al	1.96	1.96	1.98	1.96	1.78	1.69	2.83	1.24
Ti	0.01	0.00	0.00	0.00		0.09	0.02	
Fe <sup>2+</sup>	2.02	2.30	2.14	2.05	1.32	1.33	0.07	
Fe <sup>3+</sup>	0.00	0.00	0.05	0.03				
Mg	0.16	0.28	0.38	0.25	1.01	1.05	0.07	
Mn	0.32	0.06	0.33	0.61	0.00	0.00	0.00	
Ca	0.58	0.45	0.57	0.11	0.00	0.00	0.00	0.24
Na					0.02	0.03	0.17	0.62
K					0.85	0.89	0.81	0.01
X <sub>Fe</sub>					0.57	0.56		
<i>End members</i>								71.89
An								27.34
Orth								0.77
Prp	5.13	9.21	12.66	8.35				
Alm	65.26	74.09	70.77	68.69				
Grs	18.87	14.49	5.51	3.85				
Sps	10.45	1.96	10.97	19.07				

(Fig. 16e). In the SW and NE Belledonne Massif, the onset of the D<sub>2</sub> transpression with the development of S<sub>2</sub> occurred after the peak of pressure at 330 Ma (Fréville *et al.*, 2018; Jacob *et al.*, 2021), a period that corresponds to the onset of partial melting in the lower crust. In both Pelvoux and Belledonne Massifs, the transpression is more pervasive in the anatectic crust (Fréville *et al.*, 2018; this study). Melt-enhanced strength drop may have impacted stress distribution and initiated transpressional strain in the deep crust with the preferential appearance of the steeply dipping S<sub>2</sub> cleavage in the partially molten middle-lower crust, while NW-SE contraction was accommodated by upright to SE-verging D<sub>2</sub> folding in the upper-middle crust (Fig. 17).

Near the anatectic front, we have recognized a S<sub>3</sub> sub-horizontal planar fabric affecting the former S<sub>1</sub> and S<sub>2</sub> foliations (Figs. 8, 9 and 17). In sample MCE382b located in the Cortical Pelvoux, 4 monazite grains included in undeformed biotite marking the S<sub>3</sub> foliation (Figs. 10G and 10H) yield a concordant date at 306 ± 3.5 Ma (Fig. 11B). The record of the D<sub>3</sub> deformation in monazite is probably dependent on D<sub>3</sub> strain localization. Thus, we propose that the ca. 306 Ma age is a reliable one for the D<sub>3</sub> deformation in the Cortical Pelvoux (Fig. 16d). Our results suggest that during the Late Carboniferous, the D<sub>2</sub> and D<sub>3</sub> deformations were

partly synchronous (Fig. 16d) and therefore attest for strain partitioning during a same tectonic event responsible for longitudinal flow of the middle-lower crust. We interpret the top-to-the-NW shearing along S<sub>3</sub> as a local accommodation of a southeastward horizontal flow of the partially molten lower crust during sinistral transpression. Recently, Jacob (2022) and Jacob *et al.* (2022) also show that in the central Inner Pelvoux (La Lavey area) the S<sub>1</sub> foliation is reworked by a syn-migmatitic flat-lying foliation showing evidence for a NW-SE, *i.e.*, N150-N180 directed horizontal flow. These authors argue that the horizontal flow was coeval with a sinistral shearing along a N140-N170 directed high-strain corridor (D<sub>2</sub>) characterized by a vertical shortening of the D<sub>2</sub> planar fabrics by the syn-magmatic flat-lying foliation. This is consistent with our own field observations of the S<sub>3</sub> foliation, made in the same La Meije block, a few kilometers to the SE (Fig. 3). The contemporaneity between NW-SE directed transpressional flow and vertical shortening in that part of the la Meije block is supported by our radiometric data of D<sub>2</sub> and D<sub>3</sub> and attests for strain partitioning between the suprastructure and infrastructure during horizontal crustal flow under transpressive regime as commonly described in the Variscan belt (Aguilar *et al.*, 2014; Cochelin *et al.*, 2017, 2021; Rabin *et al.*, 2015; Trap *et al.*, 2017).

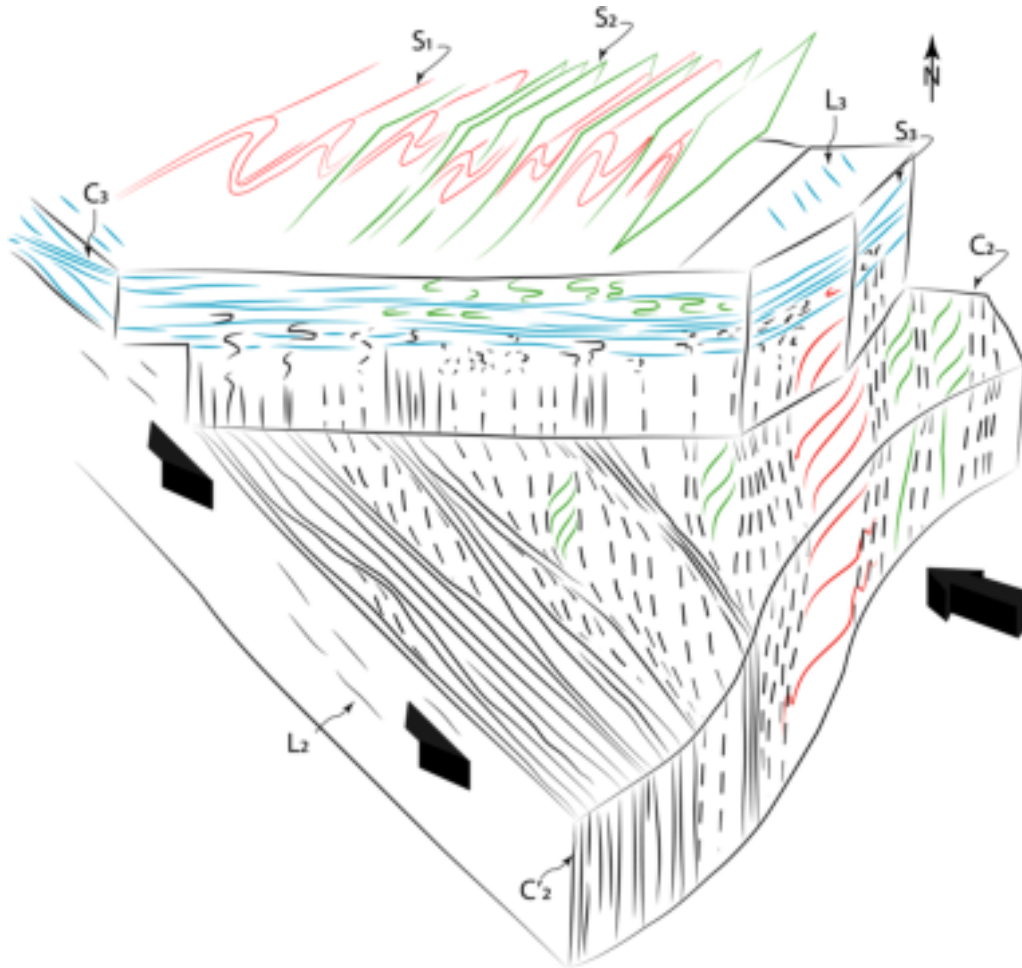


**Fig. 17.** Sketch showing the strain partitioning in the Belledonne-Pelvoux orogenic crust suffering bulk NW-SE directed contraction (black arrows). The upper unmolten crustal level recorded folding, while the partially molten lower domain recorded lateral flow and sinistral transposition.

**Table 4.** Summary of tectonic and metamorphic events recorded in the Belledonne-Pelvoux area.

Event	Belledonne SW	Cortical Pelvoux	Inner Pelvoux
<b>D3</b>			
Structure		Low angle S3 +/- mylonite Horizontal axis F3 fold and a-Type F3 fold Top to NE shearing	Low angle S3 +/- mylonitic Horizontal axis F3 fold
P-T		Retrograde amphibolite facies 0.45–0.35 GPa–450–50 °C	High-T migmatite Cordierite bearing migmatite
Age		ca. 306–298 Ma	ca. 306–298 Ma?
<b>D2</b>			
Structure	High angle S2 N030E Upright fold NE-SW axis NE-SW L2	High angle S2 N030E High angle C2 N-S High angle C'2 N150E Folded S2, Horizontal axis	High angle S2 N030E Upright fold NE-SW axis High angle C2 N-S High angle C'2 N150E NS to NE-SW L2
P-T	Sill + melt	Low-T migmatite	Low-T migmatite
Age	ca. 330–310 Ma <a href="#">Fréville et al., 2018</a>	ca. 330–298 Ma	ca. 330–298 Ma
<b>D1</b>			
Structure	Low angle S1 Recumbent fold to the east E-W L1	Mark the lithological limits low angle S1–3	Mostly erased Relictual S1 in F2 fold hinge
P-T	Amphibolite facies Grt-Bt + melt 0.6–0.8 GPa–600–630 °C	Amphibolite facies? + melt	No evidence
Age	339 ± 5 Ma	ca. 350–330 Ma	ca. 340–330 Ma? (HP stage, <i>Jacob et al., in review</i> )



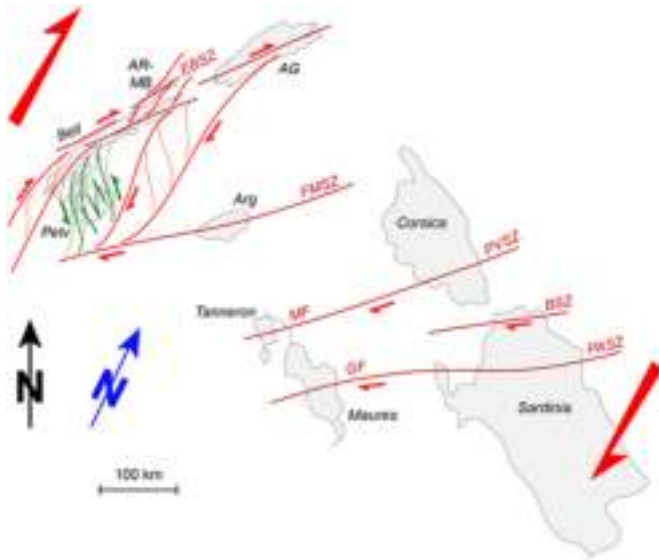


**Fig. 18.** Sketch map of the anastomosed network of dextral shear zones of the EVSZ with local conjugate sinistral shear zones in the Pelvoux Massif. Ante-alpine positions of the ECMs (black arrow) are from Bellahsen *et al.* (2014), except the Argentera Massif. Positions of the Maures-Tanneron, Corsica and Sardinia Massifs are from Edel *et al.* (2014, 2018). Blue arrow represents the present orientation in reference to the north. AG: Aar-Gothard; Arg: Argentera; AR-MB: Aiguilles-Rouges-Mont-Blanc; Bell: Belledonne; BSZ: Barrabisa Shear Zone; EBSZ: Emosson-Bérarde Shear Zone; FMSZ: Ferrière-Mollière Shear Zone; GF: Grimaud Fault; MF: La Moure Fault; PAL: Posada-Asinara Shear Zone; Pelv: Pelvoux; PVSZ: Porto Vecchio Shear Zone.

#### 5.4 Kinematic flow at the scale of the EVSZ

At large scale, the shape and strike of the EVSZ and how it connects to other major shear zones of the Variscan belt framework is not straightforward (*e.g.*, Ballèvre *et al.*, 2018; Chardon *et al.*, 2020; Simonetti *et al.*, 2020a). In most of previous studies, the authors proposed that the EVSZ runs from the Aar-Gothard, Aiguilles-Rouges-Mont-Blanc, Belledonne Massifs, and to the Argentera, Maures-Tanneron and Corsica-Sardinia Massifs with a main trend that changes from NE-SW to N-S respectively (Fig. 1; *e.g.*, Guillot *et al.*, 2009; Padovano *et al.*, 2012; Duchesne *et al.*, 2013; Simonetti *et al.*, 2020a) that consider a post-Variscan counterclockwise rotation of the Argentera Massif of about 90° that is not recorded within the Permian sedimentary cover (Bogdanoff and Schott, 1977; Sonnette *et al.*, 2014). The major rotational movements described in the internal Alps are accommodated by transcurrent faults that did not affect the ECMs (Collombet *et al.*, 2002). Any rotation of the Argentera Massif may have occurred prior to the deposition of Permian sedimentary rocks deposits and at these times the rotation in the southeastern part of the Variscan belt is clockwise (Edel *et al.*, 2014, 2015). Following the work of Edel *et al.* (2014, 2018) that consider the rotation of the Maures-Tanneron-Corsica-Sardinia block, we propose an alternative geometry for the EVSZ with the individualization of several branches forming the anastomosed network (Fig. 18).

The large-scale transpression is a strain feature the whole ECMs have in common, with a general dextral kinematics (Von Raumer *et al.*, 1999; Von Raumer and Bussy, 2004; Simonetti *et al.*, 2018, 2020a; Jacob *et al.*, 2021) except in the Pelvoux Massif where it is sinistral (this study, Strzeczynski *et al.*, 2005; Jacob *et al.*, 2022). Our results argue that the sinistral shearing in the Pelvoux Massif was active between at least ca. 320 Ma and 300 Ma. Similar ages have been reported for the dextral transpressional shearing in the Aiguilles-Rouges-Mont-Blanc Massifs (Simonetti *et al.*, 2020a; Vanardois, 2021), in the Argentera Massif (Sanchez *et al.*, 2011; Simonetti *et al.*, 2018, 2021), in the Maures-Tanneron Massifs (Rolland *et al.*, 2009; Corsini and Rolland, 2009), in Sardinia and Corsica (Giacomini *et al.*, 2008; Carosi *et al.*, 2012). Since dextral and sinistral shearing were synchronous, we propose that at the scale of the ECMs, the sinistral shearing in the Pelvoux Massif corresponds to an antithetic domain within the dextral dominated shear zone network (Fig. 18). During the Late Carboniferous times, the average antithetic C' shear zone strikes N140-150E in the Pelvoux Massif while dextral shear zones trends ca. N30E in the Aiguilles-Rouges-Mont-Blanc Massif and Belledonne Massif (*e.g.*, Simonetti *et al.*, 2020, Jacob *et al.*, 2021). Vanardois (2021) argue that N30E directed dextral deformation in the Aiguilles-Rouges Massif (Fig. 18) corresponds to 1–2 km wide synthetic C' shear zones in a regional-scale (> 10 km) N-S directed shear zone system. The strain pattern of the Aiguilles-Rouges Massif is made of a S-C-C' dextral framework with NW-SE-directed S planes, N-S directed C planes and N30E directed C' planes (Fig. 18; Vanardois 2021). In that scheme, the average obtuse angle between synthetic C' and antithetic C' shear direction might be around 105° ± 10° (Fig. 18) that is consistent with geometry and flow kinematics of a typical ductile shear zone (Fossen *et al.*, 2012; Gillam *et al.*, 2013) even if anticlockwise back-rotation between NE-SW dextral corridors is considered.

## 6 Conclusions

Our field work, structural, thermobarometric, and geochronological results argue that the Belledonne and Pelvoux Massifs share the same Carboniferous tectono-metamorphic evolution. The Belledonne-Pelvoux area experienced a D<sub>1</sub> event related to crustal thickening during the Eastward nappe stacking event in response to E-W to NW-SE contraction. The D<sub>1</sub>/M<sub>1</sub> episode ended with the onset of crustal partial melting at ca. 650 °C during Late Viséan time. Ongoing NW-SE bulk shortening is responsible for sinistral D<sub>2</sub> shearing in the partially molten middle-lower crust (*i.e.*, Inner Pelvoux) with the strain partitioning between C and C' shear zones and horizontal longitudinal flow in the range 330–300 Ma. Field and radiometric data argue for contemporaneity between D<sub>2</sub> and D<sub>3</sub> and attest for vertical strain partitioning between the suprastructure and infrastructure during horizontal crustal flow and strike-slip shearing, as commonly described in the Variscan belt. Within the orogen scale dextral East-Variscan Shear Zone, the sinistral transpression recorded in the Pelvoux Massif corresponds to an antithetic strain domain. Plate-scale kinematics and compatibility of crustal shear zones from west to east of the variscan belt are beyond the scope of this paper.

## Supplementary Material

**Figure S1.** Zircon cathodoluminescence and monazite back-scattered electrons images from studied samples.

**Table S1.** U-Pb analyses for dated samples.

**Table S2.** Operating conditions for the LA-ICP-MS equipment for Montpellier.

**Table S3.** Operating conditions for the LA-ICP-MS equipment for BRGM.

**Table S4.** Operating conditions for the LA-ICP-MS equipment for Rennes.

The Supplementary Material is available at <http://www.bsgf.fr/10.1051/bsgf/2022008/olm>.

**Acknowledgments.** The authors thank the Institut des Sciences de la Terre d'Orléans (ISTO), BRGM, the Laboratoire Chrono-Environnement, and the Observatoire des Sciences de l'Univers en Région Centre (OSUC) for their financial support. We also gratefully acknowledge the French RENATECH network and its FEMTO-ST technological facility that partly supports this work.

## References

- Abrecht J, Biino GG, Mercolli I, Stille P. 1991. Mafic-ultramafic rock associations in the Aar, Gotthard and Tavetsch Massifs of the Helvetic domain in the Central Swiss Alps: Markers of ophiolitic pre-Variscan sutures, reworked by polymetamorphic events? *Schweizerische Mineralogische und Petrographische Mitteilungen*. 71: 295–300.
- Aguilar C, Liesa M, Castiñeiras P, Navidad M. 2014. Late Variscan metamorphic and magmatic evolution in the eastern Pyrenees revealed by U-Pb age zircon dating. *Journal of the Geological Society* 171(2): 181–192.
- Alcock JE, Catalán JRM, Pascual FJR, Montes AD, Fernández RD, Barreiro JG, *et al.* 2015. 2-D thermal modeling of HT-LP metamorphism in NW and Central Iberia: Implications for Variscan magmatism, rheology of the lithosphere and orogenic evolution. *Tectonophysics* 657: 21–37.
- Autran A, Cogné J. 1980. La zone interne de l'orogène varisque dans l'ouest de la France et sa place dans le développement de la chaîne hercynienne. *Géologie Eur. 26° CGI Paris Mém. BRGM* 108: 90–111.
- Ballèvre M, Manzotti P, Dal Piaz GV. 2018. Pre-Alpine (Variscan) inheritance: A key for the location of the future Valais Basin (Western Alps). *Tectonics* 37: 786–817.
- Barbey P, Marignac C, Montel JM, Macaudière J, Gasquet D, Jabbori J. 1999. Cordierite growth texture and the conditions of genesis and emplacement of crustal granitic magmas: The Velay granite complex (Massif Central, France). *J. Petrol.* 40: 1425–1441.
- Barbey P, Villaros A, Marignac C, Montel JM. 2015. Multiphase melting, magma emplacement and PT-time path in late-collisional context: The Velay example (Massif Central, France). *Bulletin de la Société géologique de France* 186(2-3): 93–116.
- Barfety JC, Gidon M, Ménot RP, Debon F, Pêcher S, Guillot S, *et al.* 2000. Notice de la carte géologique de la France, feuille Domène (773), scale 1:50 000. Orléans: BRGM.
- Barfety JC, Montjuvent G, Pêcher A, Carme F. 1988. Notice de la carte géologique de la France, feuille La Mure (821), scale 1:50 000. Orléans: BRGM.
- Barfety JC, Pêcher A, Vivier G, Demeulemeester P, Poulain PA, Vernet J, *et al.* 1982. Notice de la carte géologique de la France, feuille St-Christophe-en-Oisans (822), scale 1:50 000. Orléans: BRGM.
- Bellahsen N, Mouthereau F, Boutoux A, Bellanger M, Lacombe O, Jolivet L, *et al.* 2014. Collision kinematics in the western external Alps. *Tectonics* 33: 2013TC003453. <https://doi.org/10.1002/2013TC003453>.
- Bellanger M, Augier R, Bellahsen N, Jolivet L, Monié P, Baudin T, *et al.* 2015. Shortening of the European Dauphinois margin (Oisans Massif, Western Alps): New insights from RSCM maximum temperature estimates and 40Ar/39Ar in situ dating. *J. Geodyn.* 83: 37–64. <https://doi.org/10.1016/j.jog.2014.09.004>.
- Bellanger M, Bellahsen N, Jolivet L, Baudin T, Augier R, Boutoux A. 2014. Basement shear zones development and shortening kinematics in the Ecrins Massif, Western Alps. *Tectonics* 33: 84–111.
- Bellot JP. 2005. The Palaeozoic evolution of the Maures Massif (France) and its potential correlation with other areas of the Variscan belt: A review. *J. Virtual Explor.* 19: 1–24.
- Bodinier JL, Dupuy C, Dostal J, Carme F. 1981. Geochemistry of Ophiolites from Chamrousse Complexe (Belledonne Massif, Alps). *Contrib Miner. Pet.* 78: 379–388.
- Bogdanoff S, Menot RP, Vivier G. 1991. Les Massifs cristallins externes des Alpes occidentales françaises, un fragment de la zone interne varisque. Extern. Cryst. Massifs Fr. West. Alps Part Intern. *Variscan Zone* 44: 237–285.
- Bordet P, Bordet C. 1963. Belledonne-Grande Rousses et Aiguilles-Rouges-Mont-Blanc : quelques données nouvelles sur leurs rapports structuraux. Livre à la mémoire du professeur Fallot. *Mém. Hors Sér. Société Géologique Fr.* 1: 309–316.
- Boutoux A, Bellahsen N, Lacombe O, Verlaquet A, Mouthereau F. 2014. Inversion of pre-orogenic extensional basins in the external Western Alps: Structure, microstructures and restoration. *J. Struct. Geol.* 60: 13–29.
- Bruguier O, Bosch D, Caby R, Vitale-Brovarone A, Fernandez L, Hamor D, *et al.* 2017. Age of UHP metamorphism in the Western Mediterranean: insight from rutile and zircon inclusions in a diamond-bearing garnet magacryst (Edough Massif, Algeria). *Earth Planet. Sci. Lett.* 474: 215–225.
- Bussien Grosjean D, Meisser N, May-Leresche S, Ulianov A, Vonlanthen P. 2017. The Morcles microgranite (Aiguilles Rouges, Swiss Alps): Geochronological and geochemical evidences for a common origin with the Vallorcine intrusion. *Swiss J. Geosci.* 110: 35–49. <https://doi.org/10.1007/s00015-017-0282-3>.
- Bussy F, Von Raumer JF. 1994. U-Pb geochronology of Palaeozoic magmatic events in the Mont-Blanc Crystalline Massif, Western Alps. *Schweiz. Mineral. Petrogr. Mitt.* 74: 514–515.
- Bussy F, Péronnet V, Ulianov A, Epard JL, Von Raumer J. 2011. Ordovician magmatism in the External French Alps: witness of a peri-Gondwanan active continental margin. In: Gutiérrez-Marco JC, Rábano I, García-Bellido D, eds. *The Ordovician of the World*. Madrid: Instituto Geológico y Minero de España, Cuadernos del Museo Geominero, Vol. 14, pp. 75–82.
- Carme F. 1970. Age briovérien probable de la majeure partie des séries supposées dévono-dinantiennes et existence d'un cycle orogénique anté-hercynien, sans doute cadomien, dans la chaîne de Belledonne (Alpes française). *C. R. Acad. Sci. Paris* 271: 631–633.
- Carme F. 1965. Sur deux formations, d'origine volcanique, des schistes cristallins anté-houillers de la chaîne de Belledonne (Alpes Française). *C. R. Acad. Sci. Paris* 260: 6401–6404.
- Chardon D, Aretz M, Roques D. 2020. Reappraisal of Variscan tectonics in the southern French Massif Central. *Tectonophysics* 787: 228477.

- Carosi R, Montomoli C, Tiepolo M, Frassi C. 2012. Geochronological constraints on post-collisional shear zones in the Variscides of Sardinia (Italy). *Terra Nova* 24: 42–51.
- Chelle-Michou C, Laurent O, Moyen JF, Block S, Paquette JL, Couzinié S, *et al.* 2017. Pre-Cadomian to late-Variscan odyssey of the eastern Massif Central, France: Formation of the West European crust in a nutshell. *Gondwana Res.* 46: 170–190.
- Cochelin B, Chardon D, Denèle Y, Gumiaux C, Le Bayon B. 2017. Vertical strain partitioning in hot Variscan crust: Syn-convergence escape of the Pyrenees in the Iberian-Armoricain syntax. *Bull. Soc. Geol. Fr.* 188.
- Cochelin B, Lemirre B, Denèle Y, de Saint Blanquat M. 2021. Strain partitioning within bending orogens, new insights from the Variscan belt (Chiroulet-Lesponne domes, Pyrenees). *Tectonics* 40: e2020TC006386.
- Collombet M, Thomas JC, Chauvin A, Tricart P, Bouillin JP, Gratier JP. 2002. Counterclockwise rotation of the western Alps since the Oligocene: New insights from paleomagnetic data. *Tectonics* 21(4): 1032.
- Compagnoni R, Ferrando S, Lombardo B, Radulesco N, Rubatto D. 2010. Paleo-European crust of the Italian Western Alps: Geological history of the Argentera Massif and comparison with Mont Blanc-Aiguilles-Rouges and Maures-Tanneron Massifs. *J. Virtual Explor.* 36. <https://doi.org/10.3809/jvirtex.2010.00228>.
- Connolly JA. 2005. Computation of phase equilibria by linear programming: A tool for geodynamic modeling and its application to subduction zone decarbonation. *Earth Planet. Sci. Lett.* 236: 524–541.
- Connolly JA, Pettrini K. 2002. An automated strategy for calculation of phase diagram sections and retrieval of rock properties as a function of physical conditions. *J. Metamorph. Geol.* 20: 697–708.
- Corsini M, Rolland Y. 2009. Late evolution of the southern European Variscan belt: Exhumation of the lower crust in a context of oblique convergence. *C. R. Geosci.* 341: 214–223.
- Couzinié S, Moyen JF, Villaros A, Paquette JL, Scarrow JH, Marignac C. 2014. Temporal relationships between Mg-K mafic magmatism and catastrophic melting of the Variscan crust in the southern part of Velay Complex (Massif Central, France). *J. Geosci.* 59: 1–18.
- Debon F, Lemmet M. 1999. Evolution of Mg/Fe Ratios in Late Variscan Pultonic Rocks from the External Crystalline Massif of the Alps (France, Italy, Switzerland). *J. Petrol.* 40: 1151–1185.
- Duchesne JC, Liégeois JP, Bolle O, Vander Auwera J, Bruguier O, Matukov DI, *et al.* 2013. The fast evolution of a crustal hot zone at the end of a transpressional regime: The Saint-Tropez peninsula granites and related dykes (Maures Massif, SE France). *Lithos* 162: 195–220.
- Duisterhoef E, Lanari P. 2020. Iterative thermodynamic modelling – Part 1: A theoretical scoring technique and a computer program (Bingo-Antidote). *J. Metamorph. Geol.* 8: 527–551.
- Faure M, Mezeme EB, Duguet M, Cartier C, Talbot JY. 2005. Paleozoic tectonic evolution of medio-europa from the example of the french massif central and massif armoricain. *J. Virtual Explor.* 19: Paper 5.
- Faure M, Rossi P, Gaché J, Melleton J, Frei D, Li X, *et al.* 2014. Variscan orogeny in Corsica: New structural and geochronological insights, and its place in the Variscan geodynamic framework. *Int. J. Earth Sci. (Geol Rundsch)*. <https://doi.org/10.1007/s00531-014-1031-8>.
- Faure M, Ferrière J. 2022. Reconstructing the Variscan terranes in the Alpine basement: facts and arguments for an Alpidic orocline. *Geosciences* 12: in press.
- Fernandez A, Guillot S, Ménot RP, Ledru P. 2002. Late Paleozoic polyphased tectonics in the SW Belledonne Massif (external crystalline massifs, French Alps). *Geodin. Acta* 15: 127–139.
- Ferrando S, Lombardo B, Compagnoni R. 2008. Metamorphic history of HP mafic granulites from the Gesso-Stura Terrain (Argentera Massif, Western Alps, Italy). *Eur. J. Mineral.* 20: 777–790. <https://doi.org/10.1127/0935-1221/2008/0020-1891>.
- Fossen H, Harris LB, Cavalcante C, Archanjo CJ, Ávila CF. 2022. The Patos-Pernambuco shear system of NE Brazil: Partitioned intracontinental transcurrent deformation revealed by enhanced aeromagnetic data. *Journal of Structural Geology* 158: 104573.
- Franke W. 2000. The mid-European segment of the Variscides: Tectonostratigraphic units, terrane boundaries and plate tectonic evolution. *Geol. Soc. Lond. Spec. Publ.* 179: 35–61.
- Franke W, Cocks LRM, Torsvik TH. 2017. The Palaeozoic Variscan oceans revisited. *Gondwana Res.* 48: 257–284.
- Fréville K. 2016. The variscan orogeny in the external crystalline massifs of Belledonne and Pelvoux (French Western Alps): The role of partial melting and plutonism on the structuration of the continental crust. Doctoral dissertation, Université de Orléans, Orléans, France.
- Fréville K, Trap P, Faure M, Melleton J, Xian-Hua L, Wei L, *et al.* 2018. New structural, metamorphic and geochronological insights on the Variscan evolution in the Alpine Belledonne Massif (France). *Tectonophysics* 726: 14–42.
- Fuhrman ML, Lindsley DH. 1988. Ternary-feldspar modeling and thermometry. *Am. Miner.* 73: 201–215.
- Gärtner A, Youbi N, Villeneuve M, Sagawe A. 2017. The zircon evidence of temporally changing sediment transport – The NW Gondwana margin during Cambrian to Devonian time (Aoucert and Smara areas, Moroccan Sahara). *Int. J. Earth Sci.* 106: 2747–2769.
- Gerbault M, Schneider J, Reverso-Peila A, Corsini M. 2018. Crustal exhumation during ongoing compression in the Variscan Maures-Tanneron Massif, France – Geological and thermo-mechanical aspects. *Tectonophysics* 746: 439–458.
- Giacomini F, Dallai L, Carminati E, Tiepolo M, Ghezzi C. 2008. Exhumation of a Variscan orogenic complex: insights into the composite granulitic–amphibolitic metamorphic basement of south-east Corsica (France). *Journal of Metamorphic Geology* 26: 403–436.
- Gibery P. 1968. Découverte de « grès à trous » renfermant des schistes noirs de Valbonnais (série cristallophyllienne des Massifs Crystallins Externes dans les Alpes française). *C. R. Acad. Sci. Paris* 267: 1251–1254.
- Gidon M, Bonhomme JL, Fourneau JC, Monjuvent G, Mouterde R. 1980. Notice de la carte géologique de la France, feuille Saint-Bonnet (845), scale 1:50 000. Orléans: BRGM.
- Gillam BG, Little TA, Smith E, Toy, VG. 2013. Extensional shear band development on the outer margin of the Alpine mylonite zone, Tatar Stream, Southern Alps, New Zealand. *Journal of Structural Geology* 54: 1–20.
- Gonçalves GO, Lana C, Scholz R, Buick IS, Gerdes A, Kamo SL, *et al.* 2016. An assessment of monazite from the Itambé pegmatite district for as U-Pb isotope reference material for microanalysis and implications for the origin of the “Moacyr” monazite. *Chem. Geol.* 424: 30–50.
- Grandjean V, Guillot S, Pecher A. 1996. Un nouveau témoin de l'évolution métamorphique BP-HT post-orogénique hercynienne : l'unité de Peyre-Arguet (Haut-Dauphiné). *C. R. Acad. Sci. Sér. 2 Sci. Terre Planètes* 322: 189–195.

- Guerrot C, Debon F. 2000. U-Pb zircon dating of two contrasting Late Variscan plutonic suites from the Pelvoux Massif (French Western Alps). *Schweiz. Mineral. Petrogr. Mitt.* 80: 249–256.
- Guillot S, di Paola S, Ménot RP, Ledru P, Spalla M, Gosso G, *et al.* 2009. Suture zones and importance of strike-slip faulting for Variscan geodynamic reconstructions of the External Crystalline Massifs of the western Alps. *Bull Soc Géol Fr.* 180: 483–500.
- Guillot S, Ménot RP. 2009. Paleozoic evolution of the External Crystalline Massifs of the Western Alps. *C. R. Geosci.* 341: 253–265.
- Henk A. 2000. Foreland-directed lower-crustal flow and its implications for the exhumation of high-pressure-high-temperature rocks. *Geol. Soc. Lond. Spec. Publ.* 179: 355–368. <https://doi.org/10.1144/GSL.SP.2000.179.01.21>.
- Jacob JB. 2022. Quelle place pour les Massifs Cristallins Externes des Alpes occidentales dans l'orogénèse varisque ? PhD Thesis, Université de Grenoble.
- Jacob JB, Guillot S, Rubatto D, Janots E, Melleton J, Faure M. 2021. Carboniferous high-pressure metamorphism and deformation in the Belledonne Massif (Western Alps). *J. Metamorph. Geol.* 39: 1009–1044. <https://doi.org/10.1111/jmg.12600>.
- Jacob JB, Janots E, Guillot S, Rubatto D, Fréville K, Melleton J, *et al.* 2022. HT overprint of HP granulites in the Oisans-Pelvoux Massif: Implications for the dynamics of the Variscan collision in the external Western Alps. <https://doi.org/10.1016/j.lithos.2022.106650>.
- Jouffray F, Spalla MI, Lardeaux JM, Filippi M, Rebay G, Corsini M, *et al.* 2020. Variscan eclogites from the Argentera-Mercantour Massif (External Crystalline Massifs, SW Alps): A dismembered cryptic suture zone. *Int. J. Earth Sci.* 109: 1273–1294. <https://doi.org/10.1007/s00531-020-01848-2>.
- Kalt A, Berger A, Blumel P. 1999. Metamorphic evolution of cordierite-bearing migmatites from the Bayerische Wald (Variscan Belt, Germany). *J. Petrol.* 40: 601–627.
- Kretz R. 1983. Symbols of rock-forming minerals. *Am. Miner.* 68: 277–279.
- Lardeaux JM, Schulmann K, Faure M, Janouzek V, Lexa O, Skrzypiek E, *et al.* 2014. The Moldanubian Zone in the French Massif Central, Vosges/Schwarzwald and Bohemian Massif revisited: Differences and similarities. *Geol. Soc. Lond. Spec. Publ.* 405: 7–44. <https://doi.org/10.1144/SP405.14>.
- Ledru P, Courrioux G, Dallain C, Lardeaux JM, Montel JM, Vanderhaeghe O, *et al.* 2001. The Velay dome (French Massif Central): melt generation and granite emplacement during orogenic evolution. *Tectonophysics* 342(3-4): 207–237.
- Le Fort P. 1973. Géologie du Haut-Dauphiné cristallin (Alpes française) : études pétrologique et structurale de la partie occidentale. PhD Thesis, Université Nancy I.
- Lemoine M. 1988. Des nappes embryonnaires aux blocs basculés : évolution des idées et des modèles sur l'histoire mésozoïque des Alpes occidentales. *G-Alp.* 8: 787–797.
- Lemoine M, Bas T, Arnaud-Vanneau A, Arnaud H, Dumont T, Gidon M, *et al.* 1986. The continental margin of the Mesozoic Tethys in the Western Alps. *Mar. Pet. Geol.* 3: 179–199.
- Linnemann U, Gerdes A, Hofmann M, Marko L. 2014. The Cadomian Orogen: Neoproterozoic to Early Cambrian crustal growth and orogenic zoning along the periphery of the West African Craton-Constraints from U-Pb zircon ages and Hf isotopes (Schwarzburg Antiform, Germany). *Precambrian Res.* 244: 236–278. <https://doi.org/10.1016/j.precamres.2013.08.007>.
- Lombardo B, Colombo F, Compagnoni R, Ghiglione G, Rubatto D. 1997. Relics of pre-Variscan events in the Malinvern-Argentera Complex, Argentera Massif, Western Alps. *Quaderni di Geodinamica Alpina e Quaternaria* 4: 66.
- Manzotti P, Ballèvre M, Pujol M. 2016. Detrital zircon geochronology in the Dora-Maira and Zone Houillère: A record of sediment travel paths in the Carboniferous. *Terra Nova* 28: 279–288.
- Matte P. 1991. Accretionary history and crustal evolution of the Variscan belt in Western Europe. *Tectonophysics* 196: 309–307.
- Matte P. 2001. The variscan collage and orogeny (480–290 Ma) and the tectonic definition of the Armorica microplate: A review. *Terra Nova* 13: 122–128.
- Matte P. 2007. Variscan thrust nappes, detachment, and strike-slip faults in the French Massif Central: Interpretation of lineations. *Geol. Soc. Am. Mem.* 200: 391–402.
- Melleton J, Cocherie A, Faure M, Rossi P. 2010. Precambrian protoliths and Early Paleozoic magmatism in the French Massif Central: U-Pb data and the North Gondwana connection in the west European Variscan belt. *Gondwana Res.* 17: 13–25.
- Ménot RP. 1988a. An overview of the geology of the Belledonne Massif (External Crystalline Massifs of western Alps). *Schweiz Miner. Petrogr. Mitt* 70: 33–53.
- Ménot RP. 1988b. Magmatisme paléozoïque et structuration carbonifère du massif de Belledonne (Alpes françaises). Contraintes nouvelles pour les schémas d'évolution de la chaîne varisque Ouest-Européenne. *Mémoire et documents du centre armoricain d'étude structurale des socles*. Rennes.
- Ménot RP. 1987. Magmatismes et structuration orogénique Paléozoïques de la Chaîne de Belledonne (Massifs cristallins externes alpins). Le Domaine Sud-Occidental. *G-Alp.* 63: 55–93.
- Oberli F, Meier M, Biino GG. 1994. Time constraints on the pre-Variscan magmatic/metamorphic evolution of the Gotthard and Tavetsch units derived from U-Pb results. *Schweiz. Miner. Petrogr. Mitt.* 74: 483–488.
- Oliot E, Melleton J, Schneider J, Corsini M, Gardien V, Rolland Y. 2015. Variscan crustal thickening in the Maures-Tanneron massif (South Variscan belt, France): new in situ monazite U–Th–Pb chemical dating of high-grade rocks. *Bulletin de la Société géologique de France* 186(2-3): 145–169.
- Padovano M, Elter FM, Pandeli E, Franceschelli M. 2012. The East Variscan Shear Zone: New insights into its role in the Late Carboniferous collision in southern Europe. *Int. Geol. Rev.* 54: 957–970.
- Padovano M, Dörr W, Elter FM, Gerdes A. 2014. The East Variscan Shear Zone: Geochronological constraints from the Capo Ferro area (NE Sardinia, Italy). *Lithos* 196-197: 27–41.
- Paquette JL, Ménot RP, Peucat JJ. 1989. R.E.E., Sm-Nd and U-Pb zircon study of eclogites from the Alpine External Massifs (Western Alps) evidence for crustal contamination. *Earth Planet. Sci. Lett.* 96: 181–198.
- Paris F, Robardet, M. 1990. Early Palaeozoic palaeobiogeography of the Variscan regions. *Tectonophysics* 1977: 193–213.
- Pecher A. 1970. Étude pétrographique de la partie orientale du massif des Ecrins-Pelvoux: le socle ancien – Alpes françaises. Thesis, Faculté des Sciences de l'Université de Grenoble, pp. 151.
- Pecher A, Vialon P. 1970. Présence de gneiss du « faciès granulite » dans le noyau précambrien du massif des Écrins-Pelvoux (Alpes du Dauphiné, France). *C. R. Acad. Sci. Paris* 270: 666–668.
- Pin C, Carme F. 1987. A Sm-Nd isotopic study of 500 Ma old oceanic crust in the Variscan belt of Western Europe: The Chamrousse ophiolite complex, Western Alps (France). *Contrib. Miner. Petrol.* 96: 406–413.
- Poitrasson F, Chenery SR, Shepherd TJ. 2000. Electron microprobe and LA-ICP-MS study of monazite hydrothermal alteration: Implications for U-Th-Pb geochronology and nuclear ceramics. *Geochim. Cosmochim. Acta* 64: 3283–3297.

- Rabin M, Trap P, Carry N, Fréville K, Cenki-Tok B, Lobjoie C, *et al.* 2015. Strain partitioning along the anatectic front in the Variscan Montagne Noire Massif (southern French Massif Central). *Tectonics* 34: 2014TC003790. <https://doi.org/10.1002/2014TC003790>.
- Roger F, Respaut JP, Brunal M, Matte P, Paquette JL. 2004. Première datation U-Pb des orthogneiss ocellés de la zone axiale de la Montagne noire (Sud du Massif central) : nouveaux témoins du magmatisme ordoVICIEN dans la chaîne Varisque. *C. R. Geosci.* 336: 19–28.
- Rolland Y, Corsini M, Demoux A, 2009. Metamorphic and structural evolution of the Maures-Tanneron Massif (SE Variscan chain): Evidence of doming along a transpressional margin: *Bull. Soc. Geol. Fr.* 3: 217–230.
- Rossi P, Oggiano G, Cocherie A. 2009. A restored section of the “southern Variscan realm” across the Corsica–Sardinia micro-continent. *Comptes Rendus Géoscience* 341(2-3): 224–238.
- Rubatto D, Ferrando S, Compagnoni R, Lombardo B. 2010. Carboniferous high-pressure metamorphism of Ordovician protoliths in the Argentera Massif (Italy), Southern European Variscan belt. *Lithos* 116: 65–76. <https://doi.org/10.1016/j.lithos.2009.12.013>.
- Sanchez G, Rolland Y, Jolivet M, Bricchau S, Corsini M, Carter A. 2011. Exhumation controlled by transcurrent tectonics: the Argentera–Mercantour massif (SW Alps). *Terra Nova* 23(2): 116–126.
- Schaltegger U. 1993. The evolution of the polymetamorphic basement in the central Alps unravelled by precise U-Pb zircon dating. *Contrib. Miner. Petrol.* 113: 466–478.
- Schnapperelle S, Mezger JE, Stipp M, Hofmann M, Gärtner A, Linnemann U. 2020 Polyphase magmatic pulses along the Northern Gondwana margin: U-Pb zircon geochronology from gneiss domes of the Pyrenees. *Gondwana Res.* 81: 291–311.
- Schneider J, Corsini M, Reverso-Peila A, Lardeaux JM. 2014. Thermal and mechanical evolution of an orogenic wedge during Variscan collision: an example in the Maures-Tanneron Massif (SE France). *Geol. Soc. Lond. Spec. Publ.* 405: 313–331. <https://doi.org/10.1144/SP405.4>.
- Sergeev SA, Steiger RH. 1993. High-precision U-Pb single zircon dating of Variscan and Caledonian magmatic cycles in the Gotthard Massif, Central Swiss Alps. *Terra Nova* 5: 394–395.
- Simonetti M, Carosi R, Montomoli C, Langone A, D’Addario E, Mammoliti E. 2018. Kinematic and geochronological constraints on shear deformation in the Ferrière-Mollières Shear Zone (Argentera-Mercantour Massif, Western Alps): Implications for the evolution of the Southern European Variscan Belt. *Int. J. Earth Sci.* 107: 2163–2189. <https://doi.org/10.1007/s00531-018-1593-y>.
- Simonetti M, Carosi R, Montomoli C, Cottle JM, Law RD. 2020a. Transpressive deformation in the Southern European Variscan Belt: New insights from the Aiguilles-Rouges Massif (Western Alps). *Tectonics* 39. <https://doi.org/10.1029/2020TC006153>.
- Simonetti M, Carosi R, Montomoli C, Corsini M, Petroccia A, Cottle JM, *et al.* 2020b. Timing and kinematics of flow in a transpressive dextral shear zone, Maures Massif (Southern France). *Int. J. Earth Sci.* 109: 2261–2285. <https://doi.org/10.1007/s00531-020-01898-6>.
- Simonetti M, Carosi R, Montomoli C, Lawd RD, Cottle JM. 2021. Unravelling the development of regional-scale shear zones by a multidisciplinary approach: The case study of the Ferrière-Mollières Shear Zone (Argentera Massif, Western Alps). *J. Struct. Geol.* 149: 104399.
- Sláma J, Košler J, Condon DJ, Crowley JL, Gerdes A, Hanchar JM, *et al.* 2008. Plešovice zircon – A new natural reference material for U-Pb and Hf isotopic microanalysis. *Chem. Geol.* 249: 1–35. <https://doi.org/10.1016/j.chemgeo.2007.11.005>.
- Stampfli GM, Hochard C, Vêrard C, Wilhem C, Von Raumer JF. 2013. The formation of Pangea. *Tectonophysics* 593: 1–19.
- Stephan T, Kroner U, Romer RL. 2019. The pre-orogenic detrital zircon record of the Peri-Gondwanan crust. *Geol. Mag.* 156: 281–307. <https://doi.org/10.1017/S0016756818000031>.
- Stipp M, Stunitz H, Heilbronner R, Schmid S. 2002. Dynamic recrystallization of quartz: Correlation between natural and experimental conditions. In: De Meer S, Drury MR, De Bresser JHP, Pennock GM, eds. *Deformation mechanisms, rheology and tectonics: Current status and future perspectives*. *Geol. Soc. Lond. Spec. Publ.* 200, pp. 171–190.
- Strzeczynski P, Guillot S, Courrioux G, Ledru P. 2005. Modélisation géométrique 3D des granites stéphaniens du massif du Pelvoux (Alpes, France). *C. R. Geosci.* 337: 1284–1292.
- Tait J, Schatz M, Bachtadse V, Soffel H. 2000. Palaeomagnetism and Palaeozoic palaeogeography of Gondwana and European terranes. *Geol. Soc. Lond. Spec. Publ.* 179: 21–31.
- Tait JA, Bachtadse V, Franke W, Soffel HC. 1997. Geodynamic evolution of the European Variscan fold belt: Palaeomagnetic and geological constraints. *Geol. Rundsch.* 86: 585–598.
- Trap P, Roger F, Cenki-Tok B, Paquette JL. 2017. Timing and duration of partial melting and magmatism in the Variscan Montagne Noire gneiss dome (French Massif Central). *Int. J. Earth Sci.* 106: 453–476.
- Vanardois J. 2021. Fusion partielle, transfert de magma et partitionnement de la déformation dans la croûte tardi-orogénique. *Exemple des massifs des Aiguilles-Rouges (Alpes) et de l’Agly (Pyénées) dans la chaîne Varisque*. PhD Thesis, Université de Franche-Comté, France, pp. 487.
- Vanardois J, Roger F, Trap P, Goncalves P, Lanari P, Paquette JL, *et al.* 2022. Variscan eclogites from Aiguilles-Rouges Massif (Western Alps): Witnesses of exhumation of deep crust through strike-slip shear zone. *J. Metamorph. Geol.*
- Vanderhaeghe O, Burg JP, Teyssier, C. 1999. Exhumation of migmatites in two collapsed orogens: Canadian Cordillera and French Variscides. *Geological Society, London, Special Publications* 154(1): 181–204.
- Vanderhaeghe O, Laurent O, Gardien V, Moyen JF, Gêbelin A, Chelle-Michou C, *et al.* 2020. Flow of partially molten crust controlling construction, growth and collapse of the Variscan orogenic belt: the geologic record of the French Massif Central [Impact du fluage de la croûte partiellement fondue sur la construction, la croissance et l’effondrement de la ceinture orogénique Varisque : l’enregistrement géologique du Massif Central français]. *Bulletin de la Société géologique de France* 191(1).
- Von Raumer JF, Bussy F. 2004. Mont-Blanc and Aiguilles-Rouges: Geology of their polymetamorphic basement (External massifs, France-Switzerland): *Mémoires de Géologie (Lausanne)* 42: 1–203.
- Von Raumer JF, Albrecht J, Bussy F, Lombardo B, Ménot RP, Schaltegger U. 1999. The Palaeozoic metamorphic evolution of the Alpine External Massifs. *Schweiz. Miner. Petrog. Mitt.* 79: 5–22.
- Von Raumer JF, Stampfli GM, Bussy F. 2003. Gondwana-derived microcontinents, the constituents of the Variscan and Alpine collisional orogens. *Tectonophysics* 365: 7–22.
- Von Raumer JF, Bussy F, Scaltegger U, Schulz B, Stampfli GM. 2013. Pre-Mesozoic Alpine basements? Their place in the European Paleozoic framework. *GSA Bull.* 125: 89–108.

- Von Raumer JF, Stampfli GM, Arenas R, Martínez SS. 2015. Ediacaran to Cambrian oceanic rocks of the Gondwana margin and their tectonic interpretation. *Int. J. Earth Sci.* 104: 1107–1121.
- Villaros A, Laurent O, Couzinié S, Moyen JF, Mintrone M. 2018. Plutons and domes: The consequences of anatectic magma extraction – Example from the southeastern French Massif Central. *International Journal of Earth Sciences* 107(8): 2819–2842.
- White RW, Powell R, Holland TJB, Worley BA. 2000. The effect of TiO<sub>2</sub> and Fe<sub>2</sub>O<sub>3</sub> on metapelitic assemblages at greenschist and amphibolite facies conditions: Mineral equilibria calculations in the system K<sub>2</sub>O–FeO–MgO–Al<sub>2</sub>O<sub>3</sub>–SiO<sub>2</sub>–H<sub>2</sub>O–TiO<sub>2</sub>–Fe<sub>2</sub>O<sub>3</sub>. *J. Metamorph. Geol.* 18: 497–511.
- White RW, Powell R, Holland TJB, Johnson TE, Green ECR. 2014. New mineral activity–composition relations for thermodynamic calculations in metapelitic systems. *J. Metamorph. Geol.* 32: 261–286.

**Cite this article as:** Kévin Fréville, Pierre Trap, Jonas Vanardois, Jérémie Melleton, Michel Faure, Olivier Bruguier, Marc Poujol, Philippe Lach. 2022. Carboniferous-Permian tectono-metamorphic evolution of the Pelvoux Massif (External Crystalline Massif, Western Alps), with discussion on flow kinematics of the Eastern-Variscan Shear Zone, *BSGF - Earth Sciences Bulletin* 193: 13.